

Optimizing Topographic Boundary Conditions for East Pacific Climate Simulation

DERVLA MEEGAN-KUMAR^a, GREGORY S. ELSSAESSER^{b,c}, DAVID S. BATTISTI^d, CHRISTOPHER M. COLOSE^{b,e},
JINGBO WU^{b,f}, JARED SEXTON^a, AND JANE W. BALDWIN^{a,g}

^a Department of Earth System Science, University of California Irvine, Irvine, California

^b NASA Goddard Institute for Space Studies, New York, New York

^c Department of Applied Physics and Mathematics, Columbia University, New York, New York

^d Department of Atmospheric Sciences, University of Washington, Seattle, Washington

^e Autonomic Integra, LLC, New York, New York

^f Center for Climate Systems Research, The Earth Institute, Columbia University, New York, New York

^g Lamont-Doherty Earth Observatory, Columbia University, Palisades, New York

(Manuscript received 30 June 2024, in final form 21 January 2025, accepted 12 February 2025)

ABSTRACT: Overly smooth topography in general circulation models (GCMs) underestimates the blocking effect of the steep mountain ranges flanking the eastern Pacific. We explore the impact of this bias on common biases in Pacific climate simulation [i.e., the unrealistic cross-equatorial symmetry of near-surface winds, sea surface temperatures (SSTs), and precipitation] through sensitivity experiments with modified Central and/or South American topography in an atmosphere–ocean coupled GCM. Quantifying orographic blocking potential via the Froude number, we determine that an envelope topographic interpolation scheme best captures observed blocking patterns. Implementing envelope topography only in Central America reduced model biases as greater blocking of the trade winds warmed SST and enhanced convergence in the northeastern Pacific. Doing so additionally over the Andes improved the simulation of South Pacific circulation and the South Pacific convergence zone as stronger deflection of the westerlies intensified the South Pacific anticyclone. This mitigated convection biases in the southeast Pacific by increasing subsidence and cooling SST. However, remote impacts of the Andes exacerbated the dry bias in the northeast tropical Pacific, resulting in negligible improvement in the East Pacific double-ITCZ. We find that, due to the significant role of large-scale convergence in driving precipitation patterns, other model biases, such as cloud-radiative biases, may modulate the impact of altering topography. Our results highlight the importance of considering alternate methods for calculating model topographic boundary conditions, though the optimal interpolation scheme will vary with model resolution and the impact of topography on GCM biases can be sensitive to choices made in formulating parameterizations.

SIGNIFICANCE STATEMENT: In this study, we explore how the mountain ranges spanning Central and South America shape the climate of the Pacific by blocking large-scale midlatitude and tropical winds. We show that the height of these mountains is typically too low in climate models and that elevating them can improve patterns of rainfall, surface ocean temperatures, and near-surface winds in the Pacific. This is important because model biases in the Pacific climate limit their utility for understanding current and future climate variability. Improving the representation of blocking by mountains can thus be a simple method for reducing uncertainties in future climate projections.


KEYWORDS: Intertropical convergence zone; Pacific Ocean; South Pacific convergence zone; Orographic effects; Topographic effects; Boundary conditions

1. Introduction

General circulation models (GCMs) have long struggled to accurately simulate the hemispheric asymmetry of the eastern tropical Pacific climate. Sea surface temperatures (SSTs) in the region are greater north of the equator than south, driving a cross-equatorial pressure gradient. Due to the convergence of the easterly trade winds over the warmer ocean, the mean position of the intertropical convergence zone (ITCZ) lies in the Northern Hemisphere, around 5°N on average (Xie and Philander 1994; Philander et al. 1996; Xie 2004; Toma and Webster 2010). As a result, there are much greater convective cloud cover and higher rainfall rates in the northeastern

tropical Pacific than in the southeastern tropical Pacific (Fig. 1a). The convection within the ITCZ is collocated with the ascending branch of the Hadley circulation, a key mechanism through which local processes in the eastern tropical Pacific shape global climate (Xie 2004), underscoring the importance of accurately representing the position of the ITCZ in GCMs. Yet, rather than a single precipitation maximum situated in the northeastern tropical Pacific, GCMs typically simulate two bands of precipitation maxima that flank the equator. Successive generations of model development have yielded only marginal improvements in the so-called double-ITCZ bias (Tian and Dong 2020; Zhang et al. 2023), and it remains a persistent challenge for model developers (Fig. 1b).

The continental margin bordering the eastern Pacific south of 15°N is composed of a series of steep, narrow mountain ranges—the Sierra Madre ranges that make up the Central American Cordillera and the Andes Mountains spanning South America. By acting as orographic barriers to the prevailing winds, these ranges play a critical role in shaping the

 Denotes content that is immediately available upon publication as open access.

Corresponding author: Dervla Meegan-Kumar, dervlak@uci.edu

DOI: 10.1175/JCLI-D-24-0316.1

© 2025 American Meteorological Society. This published article is licensed under the terms of the default AMS reuse license. For information regarding reuse of this content and general copyright information, consult the AMS Copyright Policy (www.ametsoc.org/PUBSReuseLicenses).

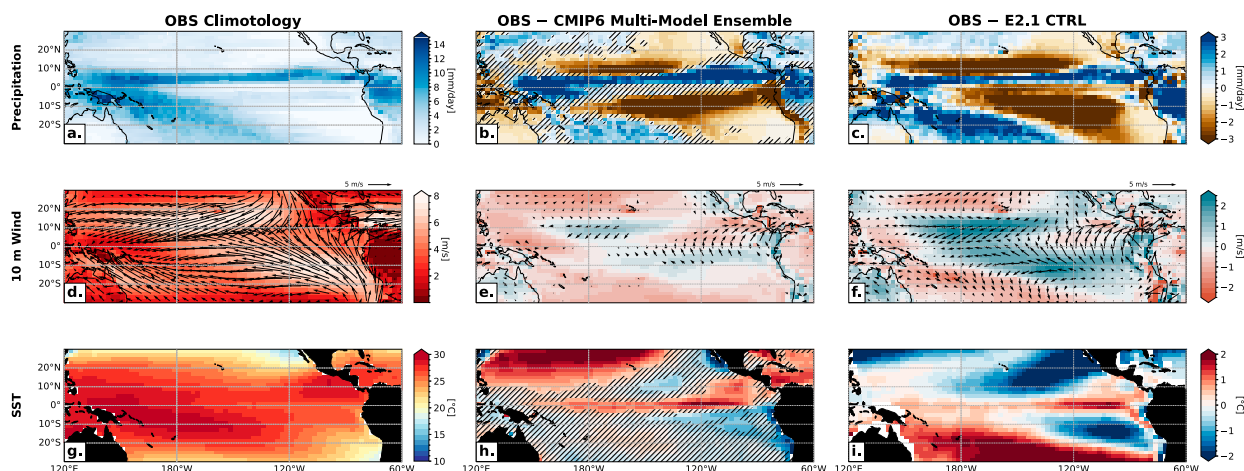


FIG. 1. Comparison between CMIP6 multimodel ensemble mean and E2.1 model biases in mean MAM climate. (left) The observed MAM climatology of (a) precipitation, (d) 10-m wind speed (shading) and velocity (vectors), and (g) SST. The biases in the (center) CMIP6 ensemble mean and (right) E2.1 model climatologies, defined as the model minus observations for (b),(c) precipitation, (e),(f) wind speed and velocity, and (h),(i) SST. The number of simulations included in the CMIP6 multimodel mean [49, 36, and 49 for (b), (e), and (h), respectively] reflects the simulations available on Pangeo at the time this figure was generated (Table A1), and hatching in (b) and (h) indicates where <75% of models agree on the sign of the bias, while the bias in wind velocity in (e) is only shown for locations where <75% of models agree on the sign of the bias.

modern climatology of the Pacific (Xie 2004; Kessler 2006; Amador et al. 2006; Espinoza et al. 2020; Fu et al. 2021). Idealized experiments with flat topography in place of the Central American Cordillera and Andes Mountains have deepened our understanding of how these orographic features dynamically and mechanically contribute to the hemispheric asymmetry of eastern Pacific climate.

In one such study, Xu et al. (2004) highlighted the importance of the northern Andes for maintaining a strong temperature inversion over the southeastern tropical Pacific Ocean. The removal of the Andes allowed warm, buoyant air masses traveling westward across the Amazon in boreal spring, which are typically blocked by the mountains, to fully traverse the continent and flow over the ocean where they contributed to the warming and destabilization of the lower atmosphere. The mechanical blocking of tropical air masses by the Andes thus typically limits the duration for which convectively favorable conditions south of the equator exist and triggers the northward seasonal migration of the ITCZ. Takahashi and Battisti (2007a), in turn, demonstrated that the Andes intersect the zonal-mean westerlies in the midlatitudes and turn the flow equatorward along downsloping isentropes where the resulting subsidence of dry air drives local SST cooling via evaporation. In their study, the impact of Andes orography on southeast Pacific SST alone was sufficient for generating the cross-equatorial pressure gradient that drives near-surface convergence north of the equator, though low-level cloud feedbacks, upwelling, and ocean heat transport provided positive feedbacks on the climatic asymmetry.

Though the prominence of the Central American Cordillera (1 km elevation, on average) is lower than that of the Andes, Xu et al. (2005) found that range is also integral in shaping the northeastern Pacific climate, particularly during boreal winter, due to the orthogonal orientation of the range

to the seasonally strengthened northeasterly trade winds. The blocking effect of the Cordillera forces the low-level flow through three topographic gaps [Tehuantepec (TE), Papagayo (PG), and Panama (PN) gaps] and air masses higher in the troposphere to flow over the range. Both of these processes suppress convection along the Pacific coast by stimulating upwelling and the entrainment of cool subsurface waters locally underneath the gap winds and subsidence-induced drying, respectively. This contributes to the offshore and southward displacement of the northern ITCZ during the Northern Hemisphere cool season. Overly strong or insufficient blocking of the northeasterly trade winds crossing Central America, however, can exaggerate these processes by leading to unrealistically low SST in the eastern Pacific warm pool (EPWP) and along the equator that drives spurious northerlies and erroneously high precipitation in the southern ITCZ (De Szoeke and Xie 2008).

These early studies were integral for demonstrating how the interaction of Central and South American topography with the mean flow shapes the background climate of the eastern Pacific such that mean convergence peaks north of the equator. Despite the importance of the Central and South American mountain ranges for eastern Pacific climate simulation, most intermediate- and coarse-resolution GCMs fail to fully capture the orographic blocking effect of these ranges as the smoothing of resolved topography results in the low bias of model surface elevation. This bias is highlighted in the studies from Xu et al. (2004, 2005) in which a regional atmosphere–ocean model exhibits significantly less flow blocking when forced with topography interpolated at a low ($T42$, $\sim 2.8^\circ$) versus high (0.5°) resolution. As the interactions between the zonal-mean flow and the orography are nonlinear, coarse-resolution models that undergo greater topographic

smoothing disproportionately suffer from the inadequate representation of peak heights (Li and Zhu 1990; Rodwell and Hoskins 2001; Takahashi and Battisti 2007a).

The most common method for interpolating high-resolution observed topography to a model grid is with a gridcell mean. This method tends to flatten out orographic features, a problem that is exacerbated at coarse resolutions (Jarraud et al. 1988; Xu et al. 2004, 2005; Elvidge et al. 2019). Improving the representation of orographic blocking without increasing horizontal resolution can thus be a simple method for reducing GCM biases without adding computational costs (Wallace et al. 1983; Baldwin et al. 2021). The numerical weather prediction community grappled with this same question some decades ago when the horizontal resolutions of weather models were comparable to the resolution of modern GCMs, $\sim 1^\circ$ to 2° . Wallace et al. (1983) tested an “envelope” technique for developing model topography that accounts for fine-scale variations of topography associated with mountain peaks and valleys by adding the standard deviation of the subgrid-scale topography to the gridcell mean. Envelope topography better captured patterns of large-scale flow blocking, particularly in winter, and thus reduced some circulation biases common among numerical weather prediction models (Wallace et al. 1983; Tibaldi 1986; Jarraud et al. 1988; Miller et al. 1989). Despite this success, the impacts of applying envelope orography as a lower boundary condition in modern GCMs have yet to be robustly evaluated.

Other seminal studies from the 1980s and 1990s alternatively implemented parameterizations of subgrid-scale orographic processes that decelerated mean wind speeds, including gravity wave breaking and surface and turbulent form drag, to partially compensate for the low resolved orography (e.g., Palmer et al. 1986; Miller et al. 1989; Lott and Miller 1997). Such parameterizations allowed for higher-fidelity representations of the topography-induced drag on the atmosphere and subgrid-scale surface stress. Despite the increasing sophistication of these parameterized schemes in modern GCMs, they may still underestimate the impact of mountains at coarse resolutions compared to explicitly resolved orographic drag, particularly over horizontally extensive orographic regions with complex terrain such as the Andes (Vosper et al. 2016; Van Niekerk et al. 2018; Vosper et al. 2020). Furthermore, differences in the subgrid-scale orography used to develop these parameterizations (Elvidge et al. 2019) and a lack of a unified characterization of the drag processes underlying these parameterizations lead to a significant intermodel spread in orographic drag parameterizations and their impact on atmospheric flow (Sandu et al. 2016, 2019; van Niekerk et al. 2020). Ultimately, refining both the parameterization of subgrid-scale orographic drag and the distribution of resolved orography is necessary to optimally reduce model biases associated with the impact of orography on the atmosphere (Miller et al. 1989; White et al. 2021); in this study, we focus on the latter.

Prior work has attempted to identify the optimal configuration of resolved topography of key mountainous regions, such as the Andes, by incrementally increasing their elevation in a series of successive model simulations and evaluating the impact on model biases (e.g., Takahashi and Battisti 2007b;

Insel et al. 2010; Xu and Lee 2021). Takahashi and Battisti (2007b) found large changes in circulation by elevating surface height from 0 to 3 km but diminishing impacts of orography > 3 km and thus concluded that a mean surface height of 3 km was sufficient for capturing the bulk of the mechanical impacts of the Andes in the Simplified Parameterizations, Primitive Equation Dynamics (SPEEDY) model. Xu and Lee (2021), however, found that circulation in CESM1.2.2 responded continually to successive increases in Andes elevation between 0 and 6 km and that the circulation associated with the Andes at elevations of 5 and 6 km was most consistent with observations. No comparable experiment exists for Central America, though Baldwin et al. (2021) tested the impact of applying gridcell maximum topographic heights in the $0.5^\circ \times 0.5^\circ$ GFDL CM2.5-FLOR model (hereafter CM2.5-FLOR) and an idealized topographic profile over Central America that preserves the gap wind regions in the $1^\circ \times 1^\circ$ CCSM4 model and found both modifications reduced biases in the northeastern Pacific by generating more realistic patterns of orographic blocking.

There are two outstanding questions regarding the role of topographic biases in Central and South America on common biases in the simulated climate in the tropical Pacific that we address with this study. 1) We explore whether using a dynamical quantity that measures orographic blocking is informative for selecting the optimal topographic interpolation scheme and can provide an objective method for developing model surface height boundary conditions. 2) While prior studies have linked model biases, including the double-ITCZ bias, to Central American and South American topography separately, the relative impact of elevated topography in these regions on Pacific circulation when modified simultaneously is unknown. For (1), we quantify the magnitude of orographic blocking by the Froude parameter to determine the optimal topographic boundary condition for reducing model biases in the eastern tropical Pacific. For (2), we use sensitivity experiments in which the selected boundary condition is applied over Central America only or over Central and South America to evaluate the relative effects of the two orographic regions on eastern Pacific climatology. We performed this series of experiments with the National Aeronautics and Space Administration (NASA) Goddard Institute for Space Studies (GISS) ModelE version 2.1-G (hereafter E2.1). To our knowledge, the role of orography on Pacific climate biases has yet to be tested with the E2.1 model, so these simulations provide an additional point of comparison for understanding the diversity of model response to orography. We only address the effects of modifying resolved topography and leave gravity wave drag and surface roughness parameterizations unchanged. Our analyses confirm that standard methods of developing model surface height boundary conditions underestimate the mechanical effects of orography. Elevating topography in the orographic regions of Central and South America improves some aspects of eastern Pacific climate simulation in E2.1, yet other model biases, such as tropical SST or subtropical stratocumulus cloud cover, can attenuate the impact.

2. Methods

a. Observed datasets

To understand the impact of modified topography on the biases in the E2.1 model, we evaluate our simulation results against various reanalysis and satellite data products. Eastward U and northward V wind components, specific humidity, atmospheric temperature, geopotential height, and low cloud cover are from reanalysis of the 1980–2022 monthly mean climate from the NASA Modern-Era Retrospective Analysis for Research and Applications, version 2 (MERRA-2, $1^\circ \times 1^\circ$ resolution; [Gelaro et al. 2017](#)). Data from satellite products include 1870–2019 monthly mean SST from the Hadley Centre Sea Ice and SST dataset (HadISST $1^\circ \times 1^\circ$ resolution; [Rayner et al. 2003](#)); 2000–19 monthly mean precipitation from the NASA Integrated Multi-satellitE Retrievals for Global Precipitation Measurement (IMERG, 30-min resolution; [Huffman et al. 2015](#)); and 2000–21 monthly mean radiation fluxes from the NASA Clouds and the Earth's Radiant Energy System Energy Balanced and Filled (CERES-EBAF) top-of-atmosphere product (Edition 4.1, $1^\circ \times 1^\circ$ resolution; [Loeb et al. 2018](#)). Mean climatologies for all satellite and reanalysis data were calculated at their native resolutions and subsequently smoothed to the E2.1 grid prior to comparison with the model simulations.

b. Model description and control simulation biases

E2.1 has 40 vertical layers in both the ocean and the atmosphere (model top of 0.1 hPa), with a horizontal resolution of 2° latitude \times 2.5° longitude in the atmosphere and land components and 1° latitude \times 1.25° longitude in the ocean component. The standard resolved topographic boundary condition for E2.1 is based on the National Geophysical Data Center (NGDC) 2-min gridded global relief product ETOPO02, version 2 ([National Geophysical Data Center 2006](#)), where the ETOPO02 topography was first coarsened to the model grid by taking area-weighted gridcell averages and then topography in cells with partial ocean fractions and over ice sheets and ice shelves was adjusted based on the NGDC 5-min ETOPO05 product ([National Geophysical Data Center 1993](#)). The roughness length, a separate boundary condition for surface height, was determined based on the variance of subgrid-scale topography from the U.S. Geological Survey Global 30 arc s elevation dataset (GTOPO30). A detailed description of the E2.1 core and suite of turbulence, cloud, and convective parameterization components is presented in [Kelley et al. \(2020\)](#).

We compare the biases in a preindustrial control (CTRL) simulation conducted with E2.1 as part of this study (see [section 2c](#) below) to the multimodel mean biases for an ensemble of historical simulations from phase 6 of the Coupled Model Intercomparison Project (CMIP6) for precipitation, 10-m winds, and SST in [Fig. 1](#). We chose to evaluate the model biases in wind speed and velocity relative to wind speed calculated from MERRA-2 reanalysis of U and V components rather than the satellite-based Remote Sensing

Systems version-7 (RSSv7) Merged Microwave Radiometer Data ([Remote Sensing Systems 2016](#)) or NASA Quick Scatterometer (QuikSCAT; [SeaPAC 2013](#)) observations of mean wind speed for consistency in comparing the bias field to the vectors. We find that the pattern of the difference in the model and observed wind speeds is similar for each of these products, although the magnitudes of the biases are greater when the models are compared to MERRA-2 (not shown). This may be due to underlying biases within the observational/reanalysis products themselves or a result of comparing wind speeds calculated from monthly averaged U and V components versus monthly mean wind speed that is output directly. Defining the E2.1 model biases as the difference between the preindustrial CTRL and the observations/reanalysis from the late twentieth to early twenty-first centuries does introduce some error as lower greenhouse gas forcing during the preindustrial led to an overall cooler global mean state during that period than modern day. Nevertheless, we find that the pattern and magnitude of the biases in the preindustrial CTRL conducted as part of this study are broadly consistent with the biases in the E2.1 historical simulations submitted to CMIP6, as discussed in prior work from [Kelley et al. \(2020\)](#) and [Miller et al. \(2021\)](#).

Both the CMIP6 ensemble mean and E2.1 simulate tropical Pacific climate that is overly symmetrical with respect to the equator, featuring anomalously cold SST, fast surface wind, and low precipitation north of the equator and anomalously warm SST, slow surface wind, and excessive precipitation south of the equator. In addition to the underestimation of cross-equatorial asymmetry in the eastern tropical Pacific, which is representative of the double-ITCZ bias, the biases in the southeast Pacific in the models also lead them to misrepresent the zonal asymmetry of the Pacific climate. As a result of the latter, the models' simulation of the South Pacific convergence zone (SPCZ) extends too far east into the southeast Pacific dry zone and has an overly gentle southeasterly tilt. E2.1 also has a double-ITCZ bias in the Atlantic basin; however, we chose to focus on the Pacific biases for the purposes of this study. Though the magnitude of these biases is larger in the E2.1 CTRL simulation than the CMIP6 multimodel ensemble mean, there is a clear consistency between the spatial patterns of the biases ([Fig. 1](#)) such that our experiments modifying topography in E2.1 may be broadly applicable for understanding Pacific climate biases in a range of GCMs. Furthermore, the majority of prior studies analyzing the impact of elevating topography in Central or South America have used relatively high-resolution models ($\leq 1^\circ$, cf. [Xu et al. 2004, 2005](#); [Junquas et al. 2016](#); [Xu and Lee 2021](#); [Baldwin et al. 2021](#); [Xu et al. 2022](#)). The use of the E2.1 model in this study thus provides an important point of comparison for understanding the impact of modifying resolved topography in a coarse-resolution model and models with relatively large biases in the simulation of the mean climate of the eastern Pacific. In regard to the former, this has particular relevance for longer atmosphere–ocean coupled simulations of projected or paleoclimates that are typically performed at lower horizontal resolution.

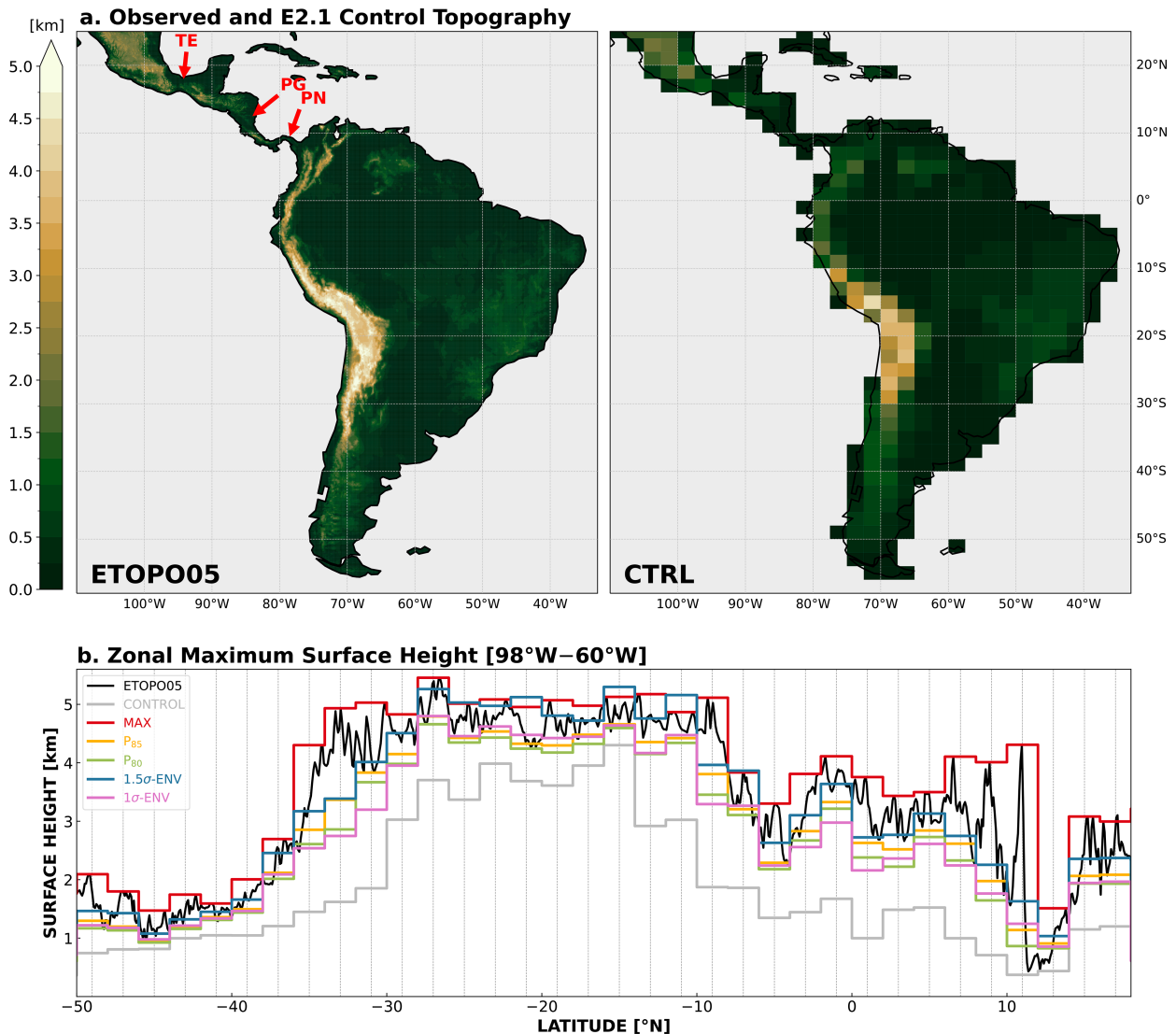


FIG. 2. Comparison of observed and model topography. (a) Distribution of topography in Central and South America for ETOPO05 observations and the E2.1 CTRL BC. Red arrows point to the TE, PG, and PN topographic gaps. (b) Latitudinal profiles of maximum surface height between 98° and 60°W for ETOPO05 (black), CTRL (gray), and a select subset of E2.1 modified surface height BCs (colors).

c. Experiments

1) MODEL SETUP

We ran a suite of preindustrial [1850 Common Era (CE)] simulations with modified resolved surface height boundary conditions (BCs) and compared these to simulations run with the standard E2.1 topography (CTRL, Fig. 2a) to evaluate the impact of orographic blocking on E2.1 biases. Preindustrial forcings—including radiative forcing, land types, and sea ice distribution—follow CMIP6 protocols (Kelley et al. 2020).

The relative sensitivity of the model to regional topography was tested with simulations in which the modified topographic BCs were applied either over both Central and South America (from 18°N to 5°S between 98° and 60°W and from 5° to 55°S between 98° and 55°W), which we refer to as CA+SA,

or only over Central America (from 18° to 5°N and 98° to 75°W), which we refer to as CA-ONLY. The CA+SA experiments address the knowledge gap on the combined impact of modifying topography in Central and South America simultaneously in GCMs. There is already considerable depth in the literature regarding the impact of elevating South American topography on model biases, yet studies offering focused analyses on the role of Central American topography are comparatively sparse. We therefore prioritized CA-ONLY experiments (as opposed to SA-ONLY) to facilitate a direct comparison to the study from Baldwin et al. (2021), which argued for outsize impacts from Central American topography.

To understand the role of atmosphere–ocean coupling on E2.1 biases, we implemented the modified topographic BCs in both AMIP-style experiments run with only the atmosphere

TABLE 1. Summary of topography modifications, applied regionally or globally, in E2.1 AGCM and AOGCM simulations. AOGCM simulations forced with 1σ ENV topography over Central America only or over both Central and South America are referred to as CA-ONLY and CA+SA, respectively, in the text.

Model	Extent of topography modification			Simulation length	Forcing protocol
	Central America only	Central and South America	Global		
AGCM	$P_{80}, P_{85}, 1\sigma$ ENV, 1.5σ ENV	$P_{80}, P_{85}, 1\sigma$ ENV, 1.5σ ENV	CTRL, MAX	30 years	1850 CE preindustrial
AOGCM	1σ ENV, MAX	1σ ENV	CTRL, MAX	350 years	1850 CE preindustrial

component of E2.1 (AGCM) and in CMIP-style experiments run with a fully coupled atmosphere–ocean GCM (AOGCM). The AGCM simulations ran for 30 years and were forced with a repeating monthly climatology of prescribed SSTs derived from HadISST observations (Rayner et al. 2003) spanning 2003–17. The AOGCM simulations were branched from an existing preindustrial control simulation with a spun-up ocean and ran for 350 years. Both the AGCM and AOGCM simulations used a “cold start” initialization of the atmosphere to generate surface pressures consistent with the modified topography. We detail the development of the modified topographic BCs in section 2c(2). Table 1 summarizes the model simulations performed for this study.

Monthly climatologies for each simulation were calculated from monthly mean output. Climatologies for the AGCM simulations include data from all of the simulation years. For the AOGCM simulations, climatologies were calculated after omitting the first 30 years of the simulation (i.e., model years 30–350). E2.1 model biases are calculated as the observations/reanalysis minus CTRL differences. The impact of the modified topographic BCs on E2.1 is quantified as the modified BC minus CTRL differences. In instances where the modified topography reduces biases in E2.1, the sign and magnitude of the differences between the modified BC simulations and CTRL will be similar to those between observations/reanalysis and CTRL. We also focus the results and discussion on March–May (MAM) seasonal means as this is when the double-ITCZ bias is strongest.

2) DEVELOPMENT OF RESOLVED TOPOGRAPHY BOUNDARY CONDITIONS

Our alternate topographic BCs are based on the NGDC 5-min gridded global relief product ETOPO05 (National Geophysical Data Center 1993; Fig. 2a left). The first method follows Xu and Lee (2021) and Baldwin et al. (2021) to develop the “MAX” BC in which gridcell average topography \bar{h} is set to be the maximum observed elevation in that grid cell from the ETOPO05 dataset h_i . Since the model grid cell is $2^\circ \times 2.5^\circ$ and the ETOPO05 dataset is on a 5-min grid, the gridcell average topography in MAX is

$$\bar{h} = H_{\max} \equiv \max(h_i), \quad i = 1, 2, \dots, 719, 720 (= 12 \times 12 \times 2 \times 2.5). \quad (1)$$

The MAX BC imposes the greatest possible mechanical blocking effect on atmospheric flow and serves as a test of the model’s sensitivity to orographic blocking.

We employed two additional methods to develop intermediate BCs where the model topography lies in between the CTRL and MAX BC end members. In the first method, we first calculate the cumulative distribution \mathcal{H} of all the ETOPO05 topographic heights h_i within that grid cell, expressed in terms of the cumulative percentage p of all h_i , $\mathcal{H} = \mathcal{H}(p)$. In this method, the grid averaged topography \bar{h} is set equal to the height at percentage $p = N$:

$$\bar{h} = H_N \equiv \mathcal{H}(p = N), \quad N = 50, 55, \dots, 90, 95. \quad (2)$$

The second method is an envelope scheme in which the grid averaged topography \bar{h} :

$$\bar{h} = H_{n\sigma} \equiv \hat{h} + n \sigma(h_i) \quad n = 0, 0.1, 0.2, \dots, 1.9, 2, \quad (3)$$

where \hat{h} is the gridcell averaged height in the ETOPO05 dataset, $\sigma(h_i)$ is the standard deviation of heights within the grid cell, and n is a scaling factor. Elevations along a north–south transect spanning the Central American Cordillera and the Andes for the ETOPO05 observations, CTRL, and selected modified BCs in Eqs. [(1)–(3)] are shown in Fig. 2b.

In total, we generated 32 candidate topographic BCs; however, running E2.1 with each possible BC would require significant computational resources and time. Instead, we selected a subset of the BCs that produced the most realistic pattern of orographic blocking based on the nondimensional Froude parameter $F = Nh/U$, where N is the buoyancy or Brunt–Väisälä frequency, h is the surface elevation, and U is the mean wind speed (Pierrehumbert and Wyman 1985; Galewsky 2009). The parameter F describes whether air flowing perpendicularly to an orographic barrier will flow over the obstacle or stagnate, where the critical value F_c at which flow stagnation occurs is approximately 1 (Baines and Smith 1993). The term F_c can vary depending on the geometry of the barrier (Smith 1989; Bauer et al. 2000) and the effects of moist dynamics on stability (Jiang 2003). For barriers that are longer than they are wide, such as the Andes or Central American Cordillera, $F_c = 1$ is a reasonable approximation (Bauer et al. 2000). This threshold thus dictates that air will flow over orography in conditions when $F \ll 1$ but will be blocked when $F \gg 1$.

We estimate the modern mean annual distribution of F using ETOPO05 topography for h and MERRA-2 reanalysis of lower-troposphere U (averaged between 1000 and 400 hPa pressure levels), potential temperature θ , and geopotential height z to calculate $N = \sqrt{(g/\theta_{600})(d\theta/dz)}$, where gravity $g = 9.81 \text{ m s}^{-2}$, θ is the potential temperature at 600 hPa, and

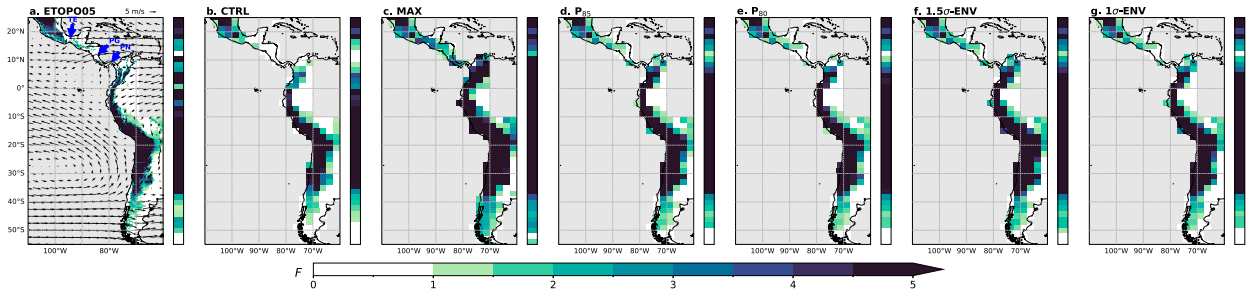


FIG. 3. Distribution and zonal maximum of orographic blocking in Central and South America based on Froude F . Patterns of orographic blocking inferred from mean annual F , calculated for (a) ETOPO05 observed topography and E2.1 topographic BCs (b) CTRL, (c) MAX, (d) P_{85} , (e) P_{80} , (f) 1.5σ ENV, and (g) 1σ ENV. To aid visualization of the interaction between topography and the low-level flow, MERRA-2 climatologies of 850-mb (1 mb = 1 hPa) winds (black vectors) and the location of the TE, PG, and PN wind gaps (bold blue arrows) are also plotted on (a). To the right of each map is a heatmap showing the maximum F value at each latitude within the domain. Cells with $F < 1$ are white. Calculation was only performed for the region where we implemented the topography modification in the model. Regions with unchanged topography are in gray, though we note that this does not necessarily mean that $F < 1$ in these cells.

$d\theta/dz$ is effectively a comparison between the environmental lapse rate and the dry-adiabatic lapse rate between the surface (1000 hPa) and the 600-hPa pressure level. Due to the generally north–south orientation of these mountain ranges and predominantly easterly/westerly orientation of the prevailing winds, we assume that the mean wind speed is a fair approximation of the cross-barrier flow. Mean values for the atmospheric state variables were calculated over regions sufficiently far upstream (1000 km) from the mountain ranges so that they are unlikely to reflect any influence of the orography (Mass and Ferber 1990; Galewsky and Sobel 2005; Galewsky 2009). As we posit that averaging observed topography to coarse-resolution model grids obscures the blocking effect of orographic barriers, the MERRA-2 climate data were disaggregated to the ETOPO05 grid prior to calculating F rather than coarsening the ETOPO05 data to the 1° MERRA-2 grid. To estimate F for our suite of potential topographic BCs, we repeated the calculation using the same quantities of U and N as above, only adjusting the values of h to reflect each topographic BC disaggregated to the high-resolution 5-min grid for consistency with the calculation of observed F .

3. Results

a. Froude number F estimates of orographic blocking

A comparison of estimated F for ETOPO05 observed topography, the CTRL BC, and a subset of modified BCs is shown in Fig. 3. The F results highlight how the E2.1 CTRL topography is insufficient for reproducing the blocking of low-level winds in Central and South America. Specifically, between 7° N and $\sim 15^\circ$ N, CTRL fails to capture the high elevations bounding the Tehuantepec, Papagayo, and Panama wind gaps (Fig. 3b). This should allow the northeasterly trade winds to traverse through an overly broad swath of the Central American continent in the model rather than being channeled through the narrow gap regions, as in observations, which may unrealistically enhance surface fluxes in the northeastern Pacific (Baldwin et al. 2021). CTRL also underestimates the blocking effect of the northern (from $\sim 0^\circ$ to 10° N)

and southern (from $\sim 32^\circ$ to 50° S) reaches of the Andes Mountains (Fig. 3b). The high elevations of the range at these latitudes are key in defining the regional circulation as this is where the prevailing tropical easterlies and midlatitude westerlies intersect with the orography (Fig. 3a). Overestimating the flow over the southern Andes may weaken the mean anticyclonic circulation in the South Pacific (Rodwell and Hoskins 2001; Takahashi and Battisti 2007a,b; Xu and Lee 2021), and the absence of blocking by the northern Andes can allow destabilizing tropical air masses flowing west across the Amazon to reach the eastern equatorial Pacific (EEP) (Xu et al. 2004). So, while at a glance the spatial patterns of F calculated with observed versus CTRL topography appear broadly similar, the underestimation of topographic heights in these three critical regions may fundamentally limit the model. The rest of our results explore the impact of elevated topography/limited blocking in these regions.

Of the 32 candidate BCs, those that most closely matched the spatial patterns of observed F are P_{80} , P_{85} , 1σ ENV, and 1.5σ ENV. The topography associated with the P_{80} , P_{85} , 1σ ENV, and 1.5σ ENV, and MAX BCs and their difference relative to CTRL are plotted in Fig. 2 and A1 in the appendix. These BCs all increase blocking over Guatemala, Honduras, and Costa Rica relative to CTRL, resulting in a more realistic representation of the peaks and valleys of the Central American Cordillera. Our Froude analysis thus quantitatively confirms the hypotheses of previous studies that the default topography in many climate models is insufficient for capturing the wind channeling effect of the Central American mountains around the Tehuantepec, Papagayo, and Panama wind gaps (Xie 2004; Xu et al. 2004; Baldwin et al. 2021). In South America, the modified BCs enhance flow blocking by the northern and southern Andes, more faithfully capturing the continental-spanning nature of the Andes. Meanwhile, MAX topography results in very high F across Central America that obscures the low-lying wind gaps and appears to unreasonably extend the width and length of the Andes across western South America (cf. Figs. 3a,c). Although prior work suggests MAX-type boundary conditions in a higher-resolution GCM

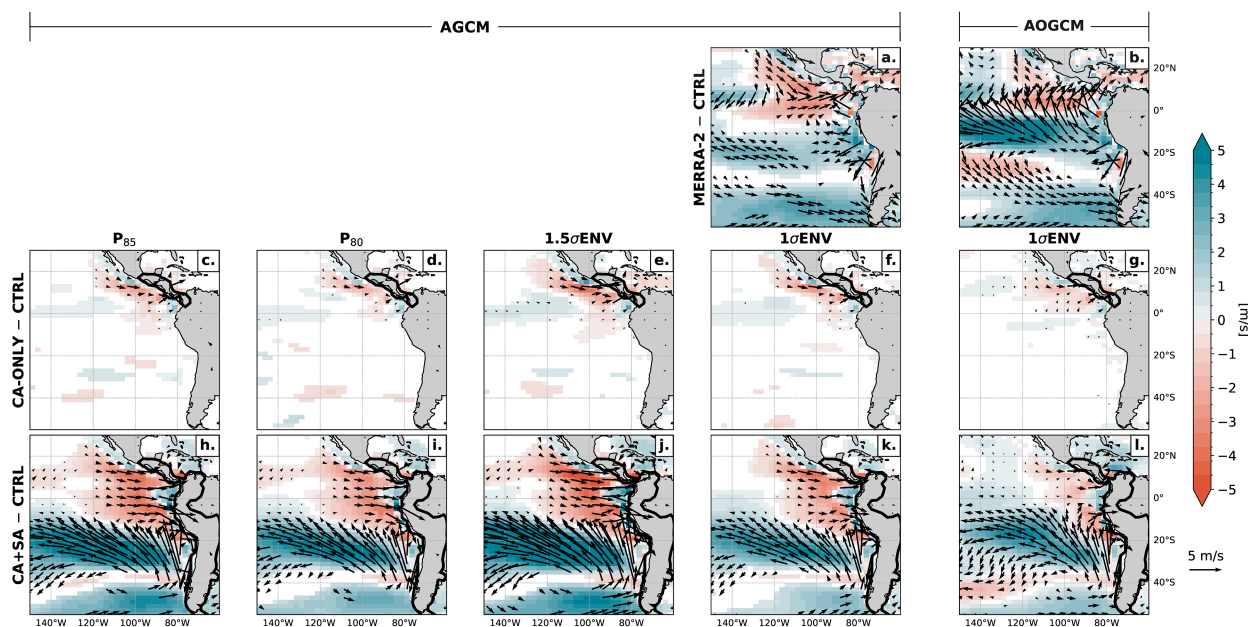


FIG. 4. Effect of topography on MAM 1000-hPa wind speeds (calculated from monthly climatologies of U and V components) and velocity (arrows). Differences between MERRA-2 reanalysis and the AGCM CTRL and (b) MERRA-2 reanalysis and the AOGCM CTRL. Differences between the modified topography simulations [(c),(h) P_{85} ; (e),(i) P_{80} ; (e),(j) 1.5σ ENV; (f),(k) 1σ ENV] and the AGCM CTRL simulation. (g),(l) Differences between the 1σ ENV AOGCM CA-ONLY and CA+SA simulations and the AOGCM CTRL simulation. The thick black contour outlines the model region in which modified topography BCs were applied either only over Central America [(c)–(g) CA-ONLY] or over both Central and South America [(h)–(l) CA+SA]. Red (blue) colors show where near-surface wind speeds in reanalysis or the modified topography simulations are slower (faster) than the (c)–(f),(h)–(k) AGCM CTRL or (g),(h) AOGCM CTRL simulations. Similarity between (c)–(l) the effect of modified topography and (a),(b) the inverse of the model bias indicates improvement in the simulation of East Pacific circulation.

improve topographic blocking, these results demonstrate that this modification is an overcorrection in the lower-resolution E2.1 as it obliterates smaller-scale but important features of the orography.

b. Impact of 1σ ENV topography on circulation in the atmosphere-only model

AGCM simulations forced with prescribed SSTs and the four selected intermediate topographic BCs (P_{85} , P_{80} , 1.5σ ENV, and 1σ ENV) provide insight into the impact of enhanced orographic blocking on low-level atmospheric circulation biases without the complication of atmosphere–ocean coupled processes. Each BC produced qualitatively similar perturbations to the 1000-hPa wind field. The redundancy ultimately reinforces our interpretation of the Froude parameter that because the modified topographic BCs have similar patterns of orographic blocking potential, they should interact with the low-level wind field consistently. Consistency between the patterns of the modified topography minus AGCM CTRL differences and the reanalysis minus AGCM CTRL differences, in turn, indicates where the elevated topography helped to reduce some of the model bias. The increased orographic blocking imposed by the elevated Central American Cordillera reduced the strength of the northeasterly trade winds over the EPWP region, with the strongest reduction in wind speeds centered at $\sim 10^\circ$ N (Figs. 4c–f). The greater prominence of the southern Andes increased the

blocking and equatorward deflection of the westerly winds impinging on the range between $\sim 35^\circ$ and 50° S, which strengthened the southerly winds flowing parallel to the Chilean coast (Figs. 4h–k). In observations, this southeasterly surface flow extends to just north of the equator (Fig. 1c). Curiously, however, there is an exacerbation of the slow wind speed bias in the tropics between $\sim 120^\circ$ to 80° W and $\sim 20^\circ$ to 5° S in all of the simulations in which both Central America and South America are elevated (Figs. 4h–k).

Though the four topographic BCs generate similar overall shifts to the surface circulation, there are some notable differences. The simulations forced with the P_{85} and 1.5σ ENV BCs, which have slightly higher mean elevations (Fig. A1), result in an excessive intensification of surface winds in the subtropical South Pacific (between $\sim 10^\circ$ and 30° S) that represents a substantial overcorrection of the $\sim 2 \text{ m s}^{-1}$ slow bias present in the AGCM CTRL simulation. Between the 1σ ENV and P_{80} BCs, the slow bias in the eastern equatorial Pacific (between $\sim 10^\circ$ S and 0°) represented by anomalous westerly winds is slightly smaller in the simulation forced with 1σ ENV topography. Given these results, in addition to the availability of previous work examining the utility of envelope topography in numerical weather prediction models (Wallace et al. 1983; Jarraud et al. 1988), we will focus the remainder of the

study on the effect of 1σ ENV topography on the atmosphere–ocean coupled version of E2.1.

c. Impact of 1σ ENV topography on circulation with a fully coupled atmosphere–ocean

The AGCM simulations show that the model's response to enhanced orographic blocking mostly follows expectations set by prior work, particularly in the nonequatorial regions of the eastern Pacific. To understand how atmosphere–ocean coupling modulates the response, we performed the same two experiments (CA-ONLY and CA+SA) with 1σ ENV modified topography and the same atmosphere coupled to a free-running ocean component (the AOGCM). Relative to the AGCM simulations, the magnitudes of the bias reduction in near-surface wind speeds generated by the 1σ ENV topography modification were modestly smaller in the AOGCM simulations (Fig. 4). Nevertheless, the spatial patterns in the 1σ ENV CA-ONLY – CTRL and CA+SA – CTRL differences in wind speed and velocity for the AOGCM experiments are more similar to the inverse model bias than the AGCM experiments (cf. Figs. 4b,g,l vs Figs. 4a,f,k). This suggests that implementing 1σ ENV topography in the AOGCM shifts the low-level wind field in the model in a manner more consistent with the observed climatology than the uncoupled model. The two most significant improvements in this pattern include the southwest–northeast trend of the reduction in wind speeds over the EPWP and the equatorward extent of the relatively fast winds between 20°S and the equator, particularly west of 100°W. Our findings are therefore generally in support of previous assertions that atmosphere–ocean coupling improves the realization of topographic modifications on model biases in the Pacific (Takahashi and Battisti 2007a; Baldwin et al. 2021; Xu et al. 2022).

In the CA-ONLY experiment, increased orographic blocking by the elevated Central American Cordillera reduces the strength of the trade winds in the northeast tropical Pacific, from the equator to 15°N (Fig. 4g). Though the bias reduction in easterly wind strength over the EPWP is $\sim 1 \text{ m s}^{-1}$ less in the AOGCM simulation than in the AGCM simulations forced with observed SST, the region of slowed winds in the coupled experiment extends southwestward from the western Central American coast toward the equator at $\sim 110^\circ\text{W}$ in a wedge-like shape that more closely matches the patterns of the inverse model bias (cf. Figs. 4a,b,g,f). Increased wind speeds to the north and south of the EPWP (including enhanced northerly flow alongshore the western Baja Peninsula that becomes northeasterly at $\sim 130^\circ\text{W}$ and southwesterly flow in the Panama basin, possibly indicating a stronger Choco low-level jet) are more aligned with observed wind speeds compared to CTRL (Figs. 4b,g). The experiments from Baldwin et al. (2021) with elevated topography over Central America in the 50-km CM2.5-FLOR and 1° CCSM4 models show similar reductions in near-surface wind biases over the northeastern Pacific, i.e., a wedge of calmer winds extending southwest from the coast toward the equator that is latitudinally bounded by regions of faster winds. Baldwin et al.

(2021) found that the elevated topography had a more pronounced impact on wind speed biases with reductions that were $\geq 1 \text{ m s}^{-1}$ greater in magnitude than in our CA-ONLY experiment, which may be due to the larger orographic blocking effect imposed by maximizing elevation in Central America relative to the envelope modification applied in this study. The consistent spatial patterns in wind speed bias reductions due to elevated Central American topography across these three different models, however, do point to the role of orographic blocking in shaping the climatology of the region as opposed to model-specific convection biases suggested by other studies (e.g., Song and Zhang 2019).

As in the AGCM simulations, the AOGCM primarily responds to elevated topography in South America by intensifying the anticyclonic circulation in the South Pacific (see Figs. 4h–l). Specifically, we observe faster southeasterlies (10°–35°S) and a stronger westerly jet (40°–50°S, east of 120°W) bounding a region of slower winds at 40°S. Though the character of these circulation shifts suggests an improvement on the too-weak subtropical circulation in the CTRL simulation, these wind changes are about 10° poleward relative to the observed biases (see Fig. 4b vs Fig. 4l). Nevertheless, atmosphere–ocean coupling seems to be important for the representation of the equatorward extent of the southeasterly winds in the South Pacific, as the AOGCM has a greater reduction in the slow wind bias in the central Pacific (between 5° and 20°S west of 100°W) than the AGCM (cf. Figs. 4k,l).

The equatorward deflection of the westerlies by the Andes should generate subsidence off the west coast of South America as the flow moves along downward-sloping isentropes (Rodwell and Hoskins 2001; Takahashi and Battisti 2007a). Indeed, we find more sinking motion in the southeast Pacific in CA+SA as a result of the elevated Andes topography (Fig. 5). This sinking is complemented by increased upward velocity over the SPCZ region in the southwest Pacific. The large amplitude oscillations in vertical velocity over the topography are likely enhanced by the lack of smoothing applied to the topography file following interpolation. Smoothing the model topography may be needed to filter high wavenumbers that introduce spurious noise (Lauritzen et al. 2015).

d. Relationship between surface circulation and SST

The surface circulation in the eastern Pacific is tightly linked to underlying SST patterns (Lindzen and Nigam 1987; Xie and Philander 1994). In the mean state, there is a steep meridional gradient between the high SST north of the equator associated with the EPWP, influenced by the Central American mountains, and the relatively cool SST along and south of the equator sustained by strong winds and shading by the low-level cloud deck, influenced by the Andes (Wallace et al. 1989). The pressure gradient resulting from this SST contrast drives strong southerly cross-equatorial winds. In the AOGCM CTRL, this hemispheric gradient is weaker relative to observations due to negative SST biases in the EPWP and positive SST

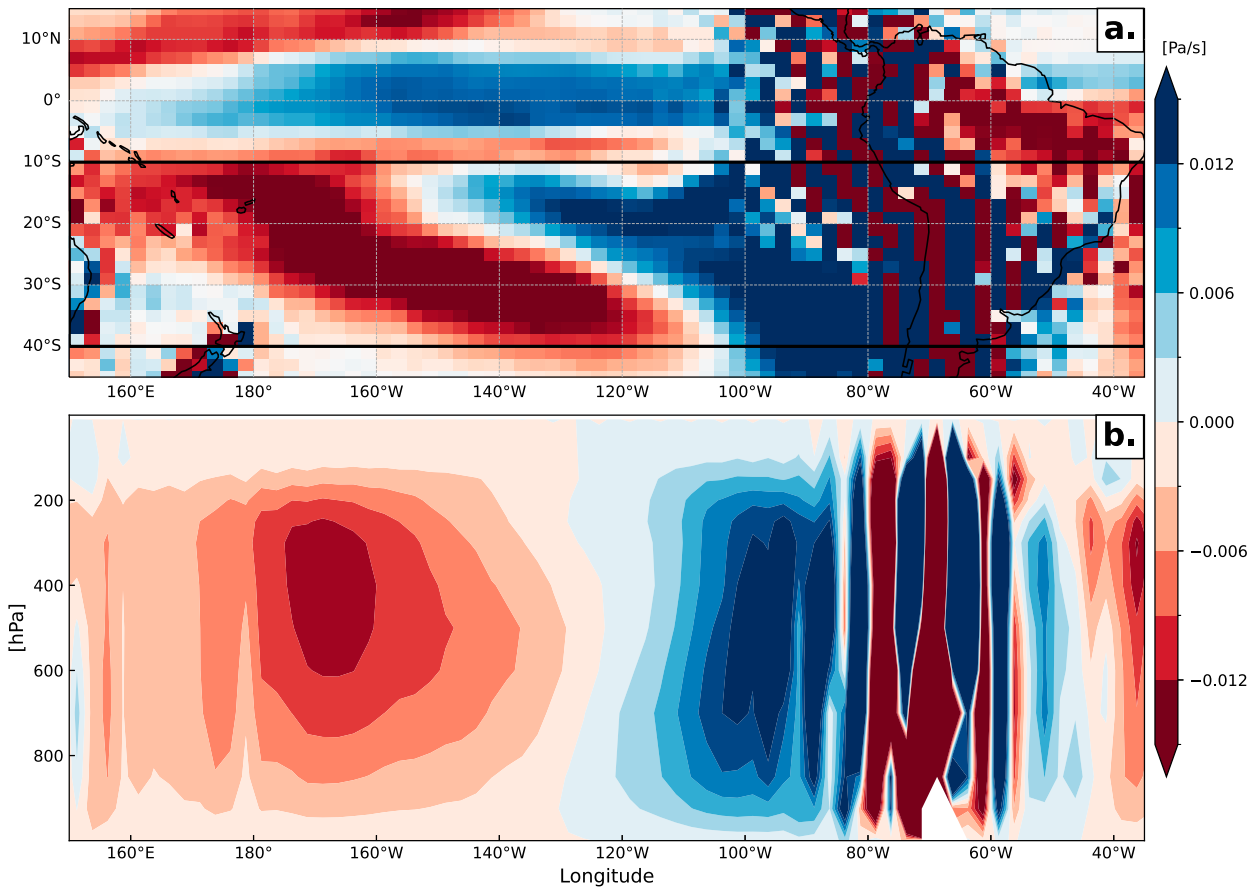


FIG. 5. Effect of Andes topography on MAM vertical velocity in CA+SA. (a) Change in vertical velocity at 500 hPa ω_{500} relative to the AOGCM CTRL; black box outlines the region averaged for lower panel. (b) Mean vertical velocity profile averaged over 40°–10°S. Red colors indicate ascent, and blue colors indicate descent.

biases in the cold tongue region (0°–20°S) and along the western coast of South America (Fig. 6a). The weak meridional SST gradient in E2.1 may thus explain the near absence of the surface southerly winds in the EEP (Table 2).

Either SST warming in the EPWP or SST cooling in the South Pacific should reduce this bias. The impact of enhanced topography on the SST bias in these two regions is addressed next.

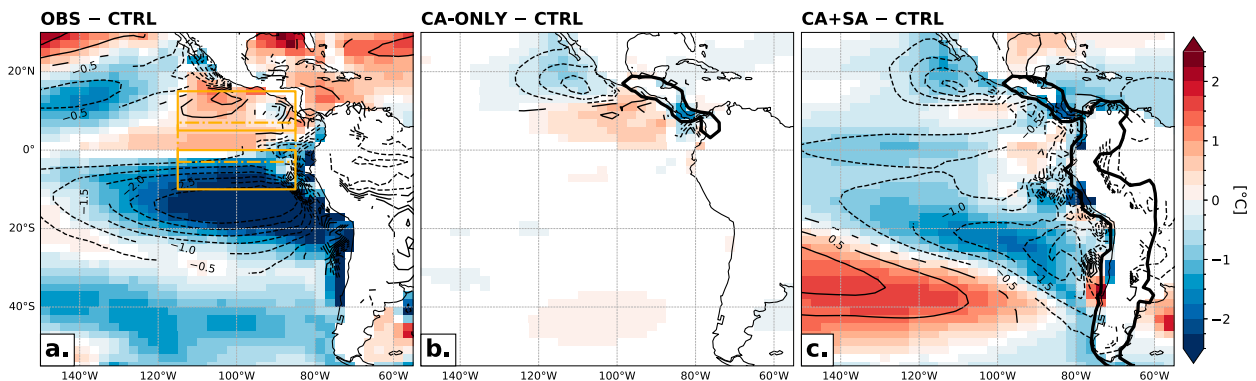


FIG. 6. Impact of topography on SST (°C; colored shading) and low-level specific humidity (g kg^{-1} ; thin black contours). Differences between the AOGCM E2.1 CTRL and (a) observations of SST from HadISST and specific humidity from MERRA-2 reanalysis, and SST and 925-hPa specific humidity fields for (b) CA-ONLY and (c) CA+SA AOGCM modified topography simulations. Thick black contours encompass the area where 1σENV topography was applied. Yellow boxes on (a) outline the regions used to calculate the mean cross-equatorial SST gradient (solid boxes) and meridional wind strength (dashed box) in Table 2.

TABLE 2. Annual and boreal spring (MAM) averaged cross-equatorial SST gradient ($N - S$ Δ SST) and equatorial 1000-hPa meridional wind strength V_{1000} for observations (HadISST and MERRA-2 reanalysis wind; OBS), the AOGCM CTRL, and the CA-ONLY and CA+SA experiments forced with 1σ ENV modified topography. The term $N - S$ Δ SST is calculated as the difference between the average SST in the EPWP (115°–85°W, 5°–15°N) minus the average SST in the EEP SST (115°–85°W, 0°–10°S) (Fig. 6a, solid gray boxes); units are in degrees Celsius (°C). The term V_{1000} is the average wind speed between 115° to 85°W and 3°S to 7°N (Fig. 6a, dotted gray box); units are in meters per second (m s^{-1}).

	Mean annual		March–May	
	$N - S$ Δ SST	V_{1000}	$N - S$ Δ SST	V_{1000}
OBS	3.50	3.38	1.35	1.69
CTRL	1.53	0.45	−0.30	−1.24
CA-ONLY	1.67	0.68	−0.04	−0.82
CA+SA	1.34	0.38	−0.32	−1.12

1) NORTHEAST PACIFIC

In the CA-ONLY experiment, solely elevating topography in Central America reduced the negative SST bias in the Pacific on the lee side of the Cordillera (Fig. 6b). The higher Cordillera increased blocking of the northeasterly trade winds east of Central America and thus reduced the high wind speed bias in the EPWP. The latter causes a local SST warming through reduced surface heat flux and reduced upwelling of subsurface waters (Baldwin et al. 2021). This effect of the range on local SST in the core of the EPWP is consistent with previous studies that improved the representation of Central American topography and associated orographic blocking—either directly by modifying the resolved surface height boundary condition (Baldwin et al. 2021) or indirectly by increasing horizontal resolution through the use of a regional model (Xu et al. 2004; Xie et al. 2007).

Baldwin et al. (2021) also found that enhanced Central American orography in CM2.5-FLOR reduced SST biases via improvements to ocean currents. In particular, better simulation of the meridional gradient in surface wind stress curl led to an eastward extension of the North Equatorial Countercurrent (NECC) which further warmed the EPWP. In E2.1, the wind stress curl gradient in the North Pacific is weak, possibly due to the limited ocean resolution of this model. Consistent with a weak wind stress curl gradient, the eastward-flowing surface current between $\sim 5^\circ$ and 10°N is very weak and largely unresponsive to the effect of Central American topography (Fig. A2). This missing NECC in E2.1 may also explain why the northeastern Pacific SST warming in response to elevated Central American topography is lower in magnitude and has a reduced westward extent in our simulations compared to CM2.5-FLOR and CCSM4 in Baldwin et al. (2021).

The effects of Central American topography on Pacific SST in CA-ONLY are limited to the northeastern tropical Pacific; there is almost no change in the AOGCM SST biases in the south of the equator (Fig. 6b). Nonetheless, the relative warming of the EPWP strengthens the cross-equatorial SST

gradient in the eastern Pacific so that it is more consistent with observations, coinciding with a modest increase in southerly wind strength crossing the equator (Table 2 and Fig. 7).

In both CA-ONLY and CA+SA, the topography modifications also reduce the positive SST bias over the Pacific southwest of the Baja Peninsula (Figs. 6b,c). The SST cooling is coincident with increased northerly winds, which represents a strengthening of the prevailing circulation.

Despite similar reductions in wind speed biases over the EPWP between 80° to 100°W and $\sim 12^\circ\text{N}$ to 0° in the CA+SA experiment (Fig. 4g), local SST warming is more moderate and confined to isolated patches when compared to the changes in CA-ONLY (Figs. 6b,c). The small region of cooler SST in the Costa Rica Dome (10°N , 90°W) relative to the surrounding EPWP is actually better simulated in CA+SA than in CA-ONLY, though this cool patch is unrealistically connected at its southwest margin to a band of low equatorial SST, a feature that is not evident in observations (cf. Figs. 6a,c). So, while the orographic blocking of the easterly trade winds by the Central American Cordillera can warm SSTs in the northeastern tropical Pacific, our results suggest that this effect is modulated by remote forcings.

A conspicuous difference between the CA-ONLY and CA+SA simulations is that Caribbean SSTs are lower in CA+SA than in the CTRL (Fig. 6c). Xu and Lee (2021) tested the impact of elevating Andes topography in the CESM1.2.2 model and also found that the topography modification led to a reduction in SST in the Caribbean and an exacerbation of the negative SST bias in the EPWP. Importantly, Xu and Lee (2021) did not alter Central American topography, so it appears that the pattern of SST change in the Caribbean is related solely to Andes topography rather than an interaction between the elevated topography of both Central and South America in CA+SA. Given advection by the prevailing easterlies, changes in SST in the Caribbean affect the temperature of the air in the EPWP region (Amador et al. 2006; Song and Zhang 2017). Alternatively, SST anomalies in the tropical North Atlantic can influence eastern Pacific SST through the remote impacts of associated diabatic heating of the atmosphere on the strength of the Walker circulation and atmospheric waves (Ham et al. 2013; Cai et al. 2019; Jiang and Li 2021). Hence, we conclude that nonlocal processes related to the effect of the Andes on the tropical Atlantic likely attenuated the reduction in SST biases over the EPWP associated with orographic blocking by the Central American Cordillera.

2) SOUTHEAST PACIFIC

In most GCMs, including E2.1, southeast subtropical Pacific SSTs are biased warm (cf. Figs. 1c,e). Elevating the Andes in CA+SA in the AOGCM counteracts some of this positive SST bias in E2.1 by creating a wedge of cooler SST that extends from the west coast of South America into the central South Pacific, northwestward from 80°W and 40°S to 140°W and 10°S (Fig. 6c). The cause of this SST cooling is likely the orographically induced subsidence of dry air that lowers SST through increased evaporative cooling (Rodwell and Hoskins 2001; Takahashi and Battisti 2007a; Xu and Lee 2021; Xu et al. 2022)

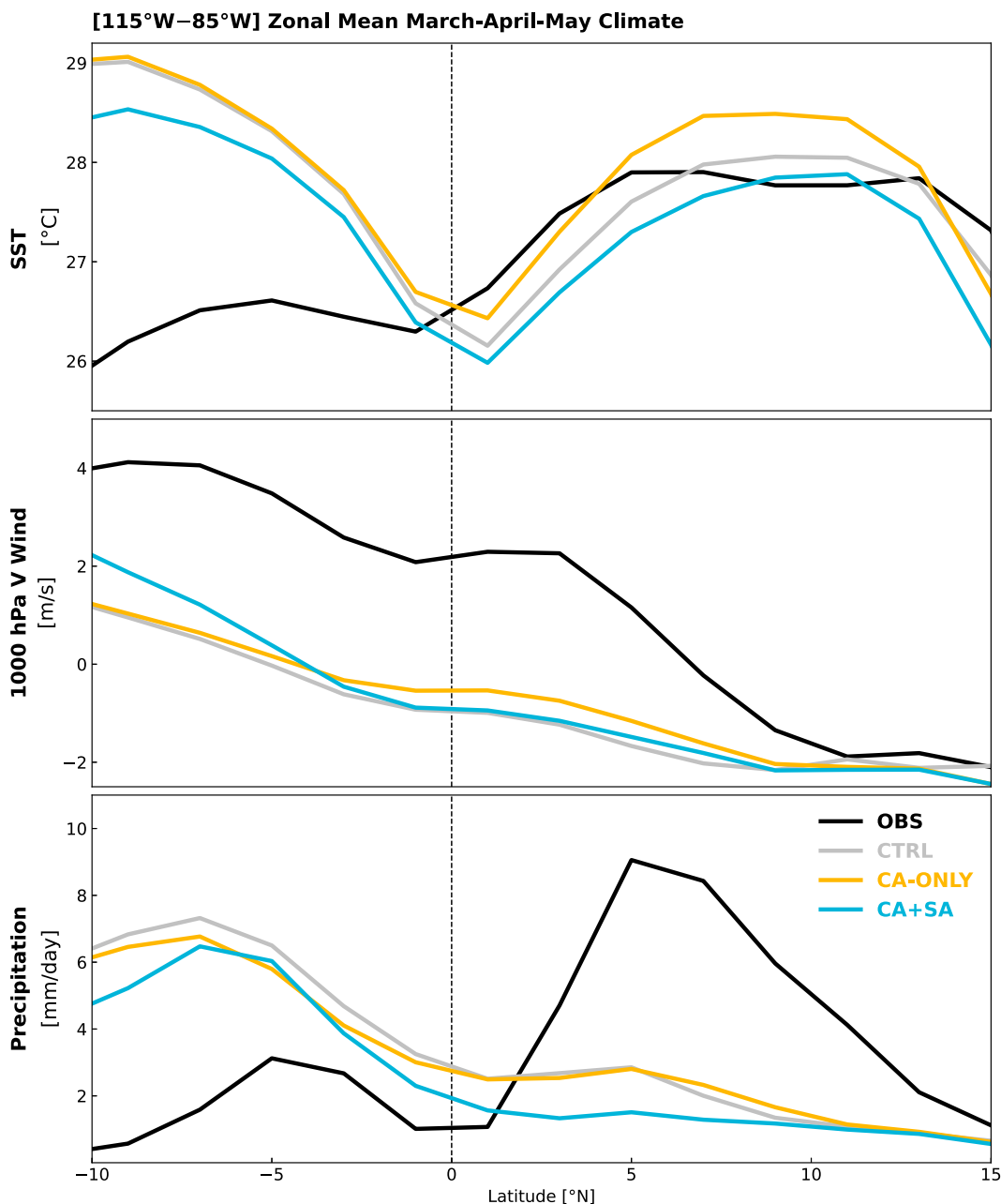


FIG. 7. Zonal-mean (115°–85°W) profile of eastern tropical Pacific climate. Latitudinal profiles of boreal spring (MAM) SST, near-surface meridional wind speed (1000 hPa V), and precipitation for observations/reanalysis (from HadISST, MERRA-2, and IMERG, respectively) and E2.1 AOGCM simulations.

as decreases in boundary layer specific humidity are collocated with the lower SSTs (Fig. 6c). As the higher Andes intensify the anticyclonic circulation in the South Pacific, the associated strengthening of the surface southeasterlies (Fig. 4l) also contributes to the enhanced evaporative cooling.

Though the wedge shape of the SST differences between CA+SA and the AOGCM CTRL is broadly similar to that of the HadISST minus AOGCM CTRL difference, the geographic location of the SST changes in CA+SA is misaligned

with the CTRL biases (cf. Figs. 6a,c). Specifically, the largest biases in the AOGCM CTRL are located immediately proximal to the Chilean coast in the subtropics (south of 20°S) and extend from the coast westward to 130°W in the tropics (between 0° and 20°S). In contrast, the strongest SST cooling in CA+SA is located at 20°–25°S between ~120° and 90°W and there is little change in the positive SST biases along the western South American coast or in the EEP east of 100°W (Fig. 6c).

The lack of equatorward extension of the SST cooling in the far eastern Pacific in CA+SA seems to follow the pattern of circulation changes that are similarly confined to the south of $\sim 10^{\circ}\text{S}$ (Fig. 4l). One possible explanation for this mismatch could be the weak subtropical cloud deck in E2.1, which we explore in greater detail in section 4a. The muted cooling within ~ 100 km of the coast in CA+SA relative to the magnitude of the CTRL biases may also be related to the coarse horizontal resolution of E2.1. da Silveira et al. (2019) found that the inability of a coarse-resolution model (1° ocean and atmosphere) to capture the northward-flowing Humboldt Current along western South America and the tendency to simulate atmospheric subsidence too low in the troposphere made SST overly sensitive to subsidence-induced warming and caused an offshore displacement of the South Pacific anticyclone. Similarly, we observe in CA+SA that the greatest increase in alongshore wind stress is displaced westward over the ocean, at $\sim 80^{\circ}\text{W}$, rather than abutting the Chilean coast (Fig. 4l). These southerly winds are important for driving offshore Ekman transport and the upwelling of cool, subsurface waters. The small change in coastal SST biases very near the coast in our E2.1 simulations could therefore be related to the absence of narrow coastal currents and the underestimation of wind-driven upwelling in the coarse-resolution model that is necessary to counteract the increased subsidence-induced warming from the enhanced flow blocking by the higher Andes.

e. Precipitation

1) IMPACT OF ELEVATED TOPOGRAPHY ON PRECIPITATION BIASES

The perturbations to circulation and SST in the modified topography experiments should alter the location and intensity of rainfall over the Pacific via their influence on surface fluxes and the convergence in low-level atmospheric moist static energy. We expect that the strengthened equatorial asymmetry in CA-ONLY will increase precipitation in the northeast Pacific ITCZ, while cooler SST and stronger subsidence over the South Pacific in CA+SA will suppress precipitation in the southeast Pacific ITCZ. Elevating the Central American Cordillera in CA-ONLY did indeed increase March–May precipitation in the northeastern ITCZ by ~ 0.5 to 1.5 mm day^{-1} , with the largest change centered at 120°W , and decrease precipitation in the southeastern ITCZ between 0° and 10°S by ~ 0.5 to 1 mm day^{-1} (Fig. 8b). While these changes marginally reduce the double-ITCZ bias in E2.1, they are small relative to the $\sim 6 \text{ mm day}^{-1}$ bias in the CTRL (Figs. 7c and 8a). In CA+SA, though the higher Andes topography does lead to additional drying in the South Pacific ITCZ region, the dry bias in the northern ITCZ (0° – 10°N) is even stronger than in CTRL and precipitation south of the equator in the central tropical Pacific is slightly increased (Figs. 7c and 8b). The circulation shifts associated with the addition of elevated topography over South America thus seem to counteract the positive effects of raising topography over Central America on the double-ITCZ bias.

Raising the height of the Andes does have a positive impact on other precipitation biases in E2.1. First, the observed distribution of precipitation in the South Pacific includes a wedge-shaped region with little deep convection extending from the South American coast northwestward (i.e., the “dry zone”) that is bounded to the southwest by the band of high precipitation extending from New Guinea to $\sim 30^{\circ}\text{S}$ and 120°W in the central Pacific (i.e., the SPCZ). Increasing the elevation of the Andes leads to a westward expansion of the dry zone by $\sim 20^{\circ}$ and a more accurate location and northwest-to-southeast tilt of the SPCZ (Fig. 8c). On land, the dipole of tropical precipitation biases over the Andes and Amazon is also slightly reduced as precipitation decreases over the mountains and increases over the Amazon, with the strongest increase in precipitation occurring along the eastern slopes of the Andes (Fig. 8c).

2) MECHANISMS DRIVING PRECIPITATION SHIFTS IN E2.1

Convection over the tropical oceans is initiated by boundary layer destabilization arising from surface latent heat fluxes (Straub and Kiladis 2002; Raymond et al. 2003, 2006) and/or the convergence of low-level moist static energy and moisture driven by pressure gradients (Battisti et al. 1999; Chiang et al. 2001; Back and Bretherton 2009b,a; Yu and Zhang 2018). Both these convection-driving processes have a first-order relationship with SST: Latent heat fluxes arise from local SST and winds, while advection and convergence processes are connected to regional SST gradients (Fu et al. 1994; Oueslati and Bellon 2013; Zhang et al. 2023). To understand how each process contributes to precipitation shifts in the CA-ONLY and CA+SA experiments, we compare in Fig. 9 the spatial patterns of the changes in latent heat flux, moisture flux convergence vertically integrated over 1000–850 hPa, and precipitation. In E2.1, there is a higher degree of coherency between the patterns of change in precipitation and low-level moisture flux convergence ($r = 0.53$ for CA-ONLY; $r = 0.39$ for CA+SA) than with change in latent heat fluxes ($r = -0.24$ for CA-ONLY; $r = -0.18$ for CA+SA). This suggests that perturbations to regional circulation, rather than local surface fluxes, exert greater influence on vertical motion and precipitation in the eastern tropical Pacific in this model. Hence, the weak SST contrast across the equator in the E2.1 CTRL and CA+SA simulations (Fig. 7a, Table 2) can account for the model’s underestimation of convergence in the northeastern tropical Pacific and thus the lack of improvement in the double-ITCZ bias in CA+SA.

The correlation between moisture flux convergence and precipitation across the central South Pacific in CA+SA (Fig. 9b) additionally supports the idea that SST gradients control the distribution of deep convection in the South Pacific through their impact on low-level moisture flux convergence (van der Wiel et al. 2016; Brown et al. 2020). Low SST and high pressure in the southeast Pacific dry zone contrast with high SST and low pressure in the western Pacific, driving moisture convergence and intense rainfall in the SPCZ region. The simulation of this zonal SST gradient is better represented in

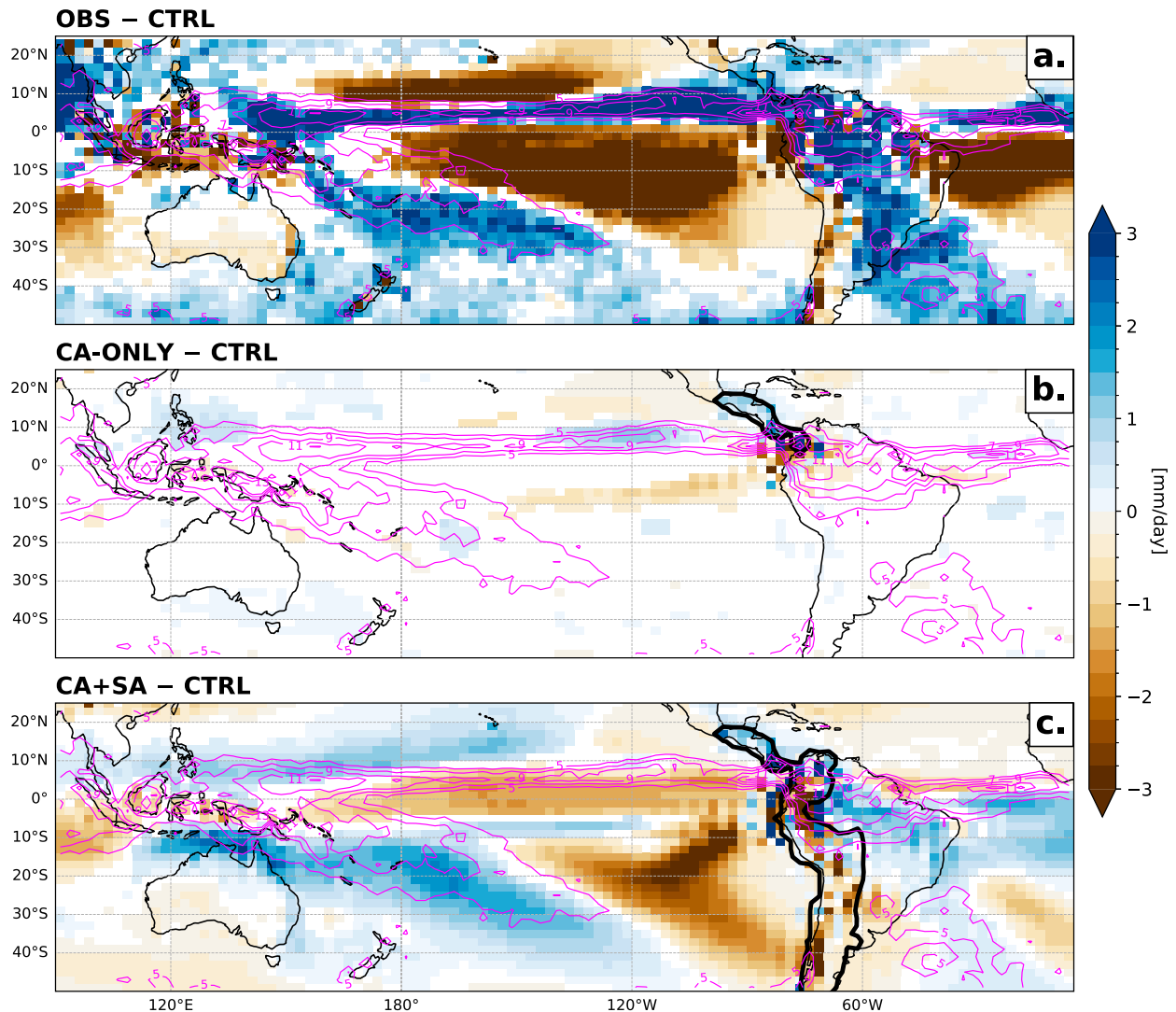


FIG. 8. Impact of enhancing Central vs South American topography on Pacific precipitation. Difference in MAM precipitation (mm day^{-1} ; shading) between the AOGCM E2.1 CTRL and (a) precipitation observations from IMERG and (b) CA-ONLY and (c) CA+SA AOGCM modified topography simulations. Observed climatological precipitation rates are shown with the fuchsia contours (contour intervals of 1 mm day^{-1} starting at 5 mm day^{-1}). Thick black contours in (b) and (c) encompass regions where 1σ ENV topography was applied.

CA+SA compared to CTRL due to enhanced evaporative cooling of SST in the southeast subtropical Pacific by the increase in the trade winds and subsidence of low specific humidity air that come about from the enhanced orography (Figs. 4l, 5b, and 6c). The southward transport and convergence of tropical moisture around the western arm of the South Pacific anticyclone, which is better captured with the elevated Andes (Fig. 4l), thus contributes to increased rainfall in the SPCZ (Fig. 8c) (Takahashi and Battisti 2007b; van der Wiel et al. 2016).

f. Impact of elevated topography on overall model biases in E2.1

We have so far focused on comparisons between model simulations to isolate the climate effect of the altered topography,

contrasting these changes with patterns of bias to highlight and explain general areas of improvement versus worsening model performance. There are locations where biases decreased in response to elevated topography, but in most locations, these improvements are minor compared to the overall model biases. To illustrate this, we take the direct difference in our simulation results and reanalysis/observations in Fig. 10. Given the limited influence of Central American topography on the broader climate biases of the eastern Pacific, we find minimal change in the root-mean-square error (RMSE) of the model biases in 1000-hPa winds (Figs. 10a,d) and SST (Figs. 10b,e) in CA-ONLY relative to CTRL, though there is a modest improvement in precipitation biases indicated by the reduction in RMSE from 3.38 to 3.29 mm day^{-1} (Figs. 10c,f). While the circulation change in

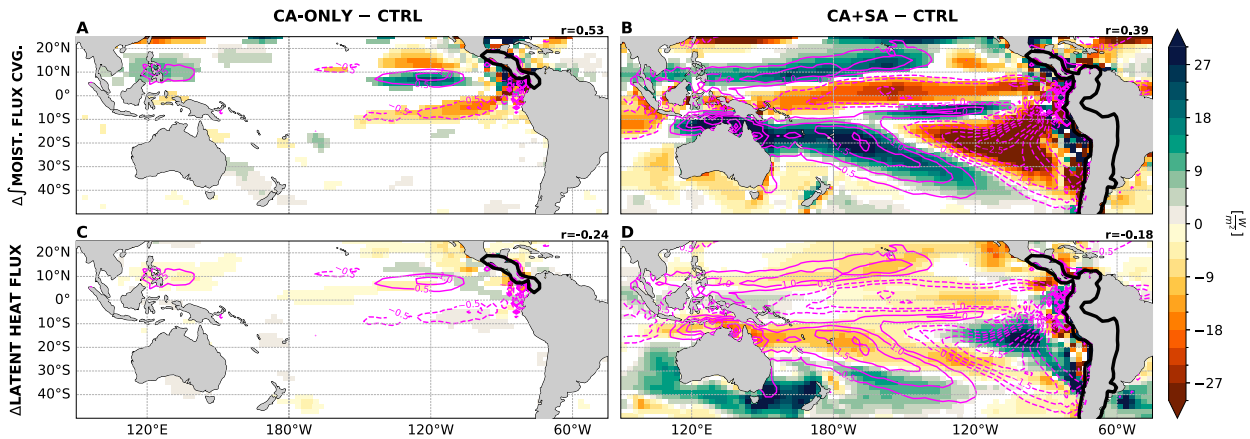


FIG. 9. Contribution of low-level moisture flux convergence and latent heat flux perturbations to the precipitation changes in E2.1 AOGCM simulations. Difference in precipitation in (left) CA-ONLY and (right) CA+SA compared to the CTRL (fuchsia contours; contour interval is 1 mm day^{-1} starting at $\pm 0.5 \text{ mm day}^{-1}$; solid lines correspond to increased precipitation, and dashed lines correspond to decreased precipitation) due to (a),(b) moisture flux convergence vertically integrated from 1000- to 850-hPa pressure levels and (c),(d) latent heat flux. Differences calculated for the MAM season.

CA+SA relative to CTRL qualitatively appears similar to the inverse model bias (Figs. 4b,l), it is shifted too far south resulting in small quantitative improvements to wind bias, reducing the RMSE of the 1000-hPa wind field from 2.25 m s^{-1} versus 2.11 m s^{-1} (Figs. 10a,g). The larger and further reaching impacts of the Andes topography in CA+SA actually result in a slight exacerbation of the overall model biases in SST and precipitation relative to CTRL (Figs. 10b,h,c,i).

4. Discussion

Overall, improvements in some locations and worsening simulation in others lead the implementation of 1σ ENV topography to not meaningfully reduce the overall regional RMSE of the model bias. By better capturing orographic blocking in Central and South America in the E2.1 AOGCM, this topographic modification does still alleviate some circulation biases in the CTRL simulation. This includes enhanced blocking of the northeasterly trade winds by the Central American Cordillera and the midlatitude westerlies in the South Pacific by the Andes. The influence of these circulation changes on precipitation biases is a more complicated picture. Elevating Central America alone only marginally improves the double-ITCZ bias, while the addition of elevated topography in South America in CA+SA actually exacerbates the dry bias in the northeast Pacific ITCZ despite improvements in the simulation of atmospheric subsidence and SST cooling in the South Pacific. The simulation of decreased precipitation in the northeast tropical Pacific ITCZ region in response to elevated Andes topography in E2.1 contrasts with the expectations from some foundational studies describing the role of the South Pacific in forcing the hemispheric asymmetry of the eastern tropical Pacific climate (Lindzen and Nigam 1987; Philander et al. 1996). Nevertheless, this result is not wholly inconsistent with other idealized modeling experiments that measured the impact of

Andes topography on the double-ITCZ bias. For example, Takahashi and Battisti (2007a) found that modifying Andes topography in the SPEEDY model only generated a single precipitation maximum in the northeastern tropical Pacific when low-cloud feedbacks were adequately parameterized. A more recent study from Xu and Lee (2021) that implemented MAX topography over the Andes in CESM1.2.2 found that the modification further reduced precipitation east of 100°W in the northeastern tropical Pacific, similar to our CA+SA results. In the rest of the discussion and conclusions, we explore some possible reasons for the limited benefit of the topographic change in E2.1 and implications for future work in light of these results.

a. Missing low-level cloud feedbacks

While we find that the impact of topography on Pacific climate biases fits with expectations in the off-equatorial regions of the eastern Pacific, the high SST and slow wind speed biases in the EEP in the control simulation are not remedied by the improved representation of orography. As these biases are spatially collocated with known low cloud biases off the coasts of the continents in eastern boundary current regions, there may be a connection between shortwave radiation biases in the model and the ability to resolve the impact of topography on the double ITCZ.

The stratocumulus cloud deck located to the west of South America provides an important feedback on the atmospheric pressure gradients that drive the mean cross-equatorial southerly flow that defines the climatic asymmetry of the eastern tropical Pacific. Prior work has linked processes or parameterizations in the atmosphere component of GCMs that result in biases in cloud radiative effects to the overly symmetric distribution of precipitation in the tropical Pacific (Wang et al. 2005; Xiang et al. 2017; Popp and Silvers 2017; Zhou and Xie 2017; Naumann et al. 2019; Zhou et al. 2022; Liu et al. 2023). The poor representation of low clouds in the EEP is a known bias in many AOGCMs, including E2.1 (Kelley et al. 2020),

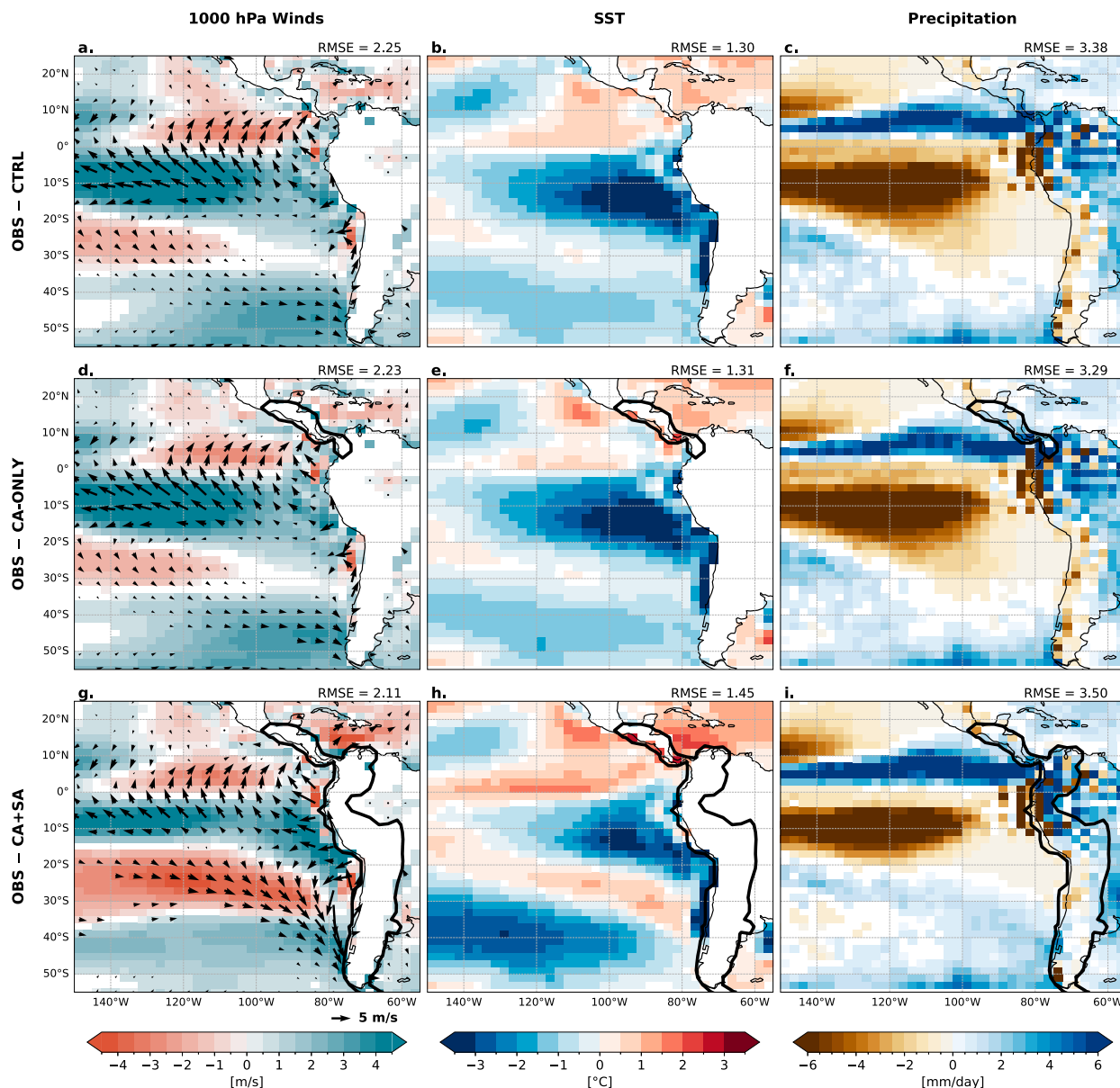


FIG. 10. AOGCM model biases for MAM across different simulations. $-1 \times$ model bias (i.e., OBS simulation) for (a)–(c) CTRL, (d)–(f) CA-ONLY, and (g)–(i) CA+SA. Biases are examined for (a), (d), (g) 1000-hPa wind speed (shaded) and velocity (arrows), (b), (e), (h) SSTs, and (c), (f), (i) precipitation. See section 2a for details of the observed datasets used. RMSE is listed in the top-right corner of each panel. Note that for the wind panels, RMSE is calculated for wind speed.

and there is a strong correlation between the related positive incoming shortwave radiation bias and the degree of equatorial asymmetry in eastern tropical Pacific precipitation (i.e., magnitude of the double-ITCZ bias) (Seo et al. 2014; Li and Xie 2014; Xiang et al. 2017). Atmosphere–ocean coupled processes, such as the wind–evaporation–SST mechanism, are likely also important for amplifying the impact of radiation biases on the double ITCZ (Xie et al. 2007; Takahashi and Battisti 2007a; Xiang et al. 2017; Kim et al. 2022).

Like many GCMs, E2.1 substantially underrepresents the effect of low clouds on underlying SST and/or lower troposphere

temperature, which likely reduces associated feedbacks on the cross-equatorial southerlies that concentrate precipitation in a band north of the equator. In E2.1, the negative bias of low cloud cover in the subtropical South Pacific corresponds to $\sim 40 \text{ W m}^{-2}$ more shortwave radiation absorbed at the surface compared to observations (Fig. 11a). Climate biases associated with low Andes topography may contribute to the weak stratocumulus cloud deck in E2.1. The mechanically induced subsidence in the South Pacific anticyclone forced by the Andes is understood to create a favorable environment for stratocumulus cloud formation by strengthening the temperature inversion

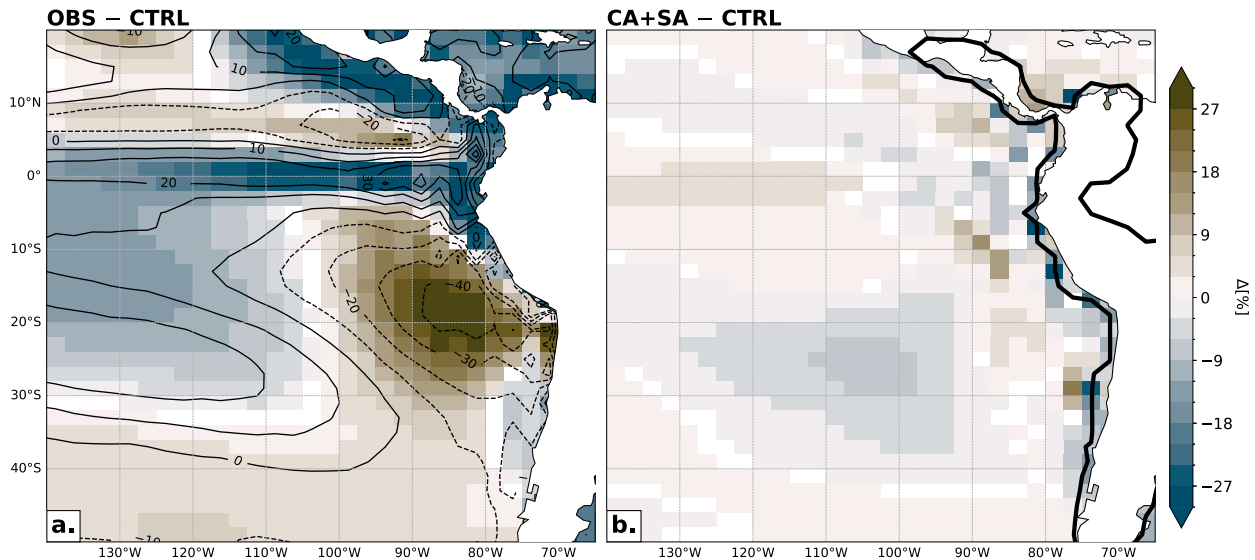


FIG. 11. Low cloud cover and associated shortwave radiation biases in E2.1. Difference in mean annual fractional low cloud cover between (a) the AOGCM CTRL and MERRA-2 reanalysis and between (b) the CA+SA and CTRL simulations (shaded). Black contours in (a) show the bias in top-of-atmosphere shortwave cloud-radiative forcing in the AGCM CTRL simulation relative to observations (CERES-EBAF; [Loeb et al. 2018](#)), where dashed (solid) contours indicate more (less) absorbed shortwave radiation in E2.1 relative to observations; contour interval is 10 W m^{-2} . The thick black contour in (b) outlines the area of elevated topography in CA+SA.

and stability of the lower troposphere ([Wang et al. 2004](#); [Xu et al. 2004](#)). Cloud-radiation feedbacks, including enhanced reflection of incoming shortwave radiation and stronger cloud-top cooling by outgoing longwave radiation, in turn, generate a diabatic enhancement of the inversion strength ([Rodwell and Hoskins 2001](#); [Wang et al. 2004](#); [Myers and Norris 2013](#)). While we do observe that the elevated Andes increased SST cooling ([Fig. 6c](#)) and subsidence ([Fig. 5](#)) in the southeast Pacific, the difference in low-level cloud cover in CA+SA relative to the AOGCM CTRL is negligible ($\sim 4\%$) ([Fig. 11b](#)). The lack of change in low cloud cover in CA+SA despite the more favorable environment for low cloud formation may be due to fundamental limitations of E2.1, most notably the coarser vertical resolution in the planetary boundary layer and/or turbulence and stratiform microphysics schemes ([Kelley et al. 2020](#)).

Poor simulation of the subtropical stratus clouds contributing to too much simulated precipitation in the EEP is consistent with previous work. [Takahashi and Battisti \(2007a\)](#) were only able to fully capture the impact of Andes topography on Pacific climate asymmetry (i.e., northerly position of the eastern Pacific ITCZ) in their study with the SPEEDY model after modifying the standard configuration of the model to optimize for low cloud simulation. More recently, [Woelfle et al. \(2019\)](#) found that the improvement of subtropical cloud physics in the CESM2 model decreased the model's double-ITCZ bias in the Pacific compared to earlier generations of the model. As the recently completed GISS ModelE Version 3 (E3) includes updated physics and tuning for simulating low-level clouds ([Cesana et al. 2019](#); [Elsaesser et al. 2025](#)), in addition to higher vertical resolution that may improve the representation of boundary layer processes and the sensitivity of low-level clouds to shifts in the boundary layer environment

([Bony and Dufresne 2005](#)), Andes topography may more substantially influence double-ITCZ biases in E3 than E2.1. In short, it is possible that both process-based cloud biases and topographic biases might need to be improved in concert to improve the double ITCZ.

b. Global application of MAX topography

While our study focused on the impact of mountains east of the Pacific on model biases in E2.1, our results raise the question of whether enhancing orographic blocking by implementing model topography that better captures peak heights globally improves model simulations of climate in other regions. [Baldwin et al. \(2021\)](#) tested the impact of maximizing the orographic blocking in the CM2.5-FLOR model (a relatively high-resolution 50 km model) through the global implementation of the MAX topographic interpolation scheme. Interestingly, they found that the application of MAX topography globally versus only over Central America yielded similar reductions in Pacific climate biases. This led the authors to conclude that capturing the magnitude of Central American orographic blocking is critical for accurately simulating aspects of climate on a global scale due to its outsized effect on ITCZ position and El Niño–Southern Oscillation variability.

To determine whether other orographic regions beyond Central and South America exert a greater influence on E2.1 biases, we ran an additional AOGCM simulation with E2.1 in which MAX topography was implemented in each model grid cell ($\text{MAX}_{\text{global}}$). $\text{MAX}_{\text{global}}$ had a more substantial impact on E2.1 climate simulation than either the changes to regional orography implemented in CA-ONLY or CA+SA. This is exemplified by the changes in mean annual SST, notably the dipole of SST cooling and warming in the North and South

Atlantic, respectively (Fig. 12a). This SST pattern is reminiscent of deglacial paleoclimates in which enhanced freshwater fluxes to the North Atlantic force a weakening of the Atlantic meridional overturning circulation (AMOC) and southward shift in the latitudinal position of the ITCZ (Timmermann et al. 2007; Chiang and Friedman 2012). Indeed, as measured by the maximum in the streamfunction at ~ 1000 -m depth in the North Atlantic, the AMOC is 20 Sv ($1 \text{ Sv} \equiv 106 \text{ m}^3 \text{ s}^{-1}$) lower in $\text{MAX}_{\text{global}}$ relative to the AOGCM CTRL, suggesting that the anomalous SST pattern in $\text{MAX}_{\text{global}}$ is due to a collapse of AMOC (Fig. 12b). Basin-mean northward heat transport in the Atlantic declined immediately from the simulation start (Fig. 12c), pointing to the role of atmospheric processes in driving the change in AMOC. We compared the surface temperature and precipitation response of the E2.1 AOGCM and AGCM to $\text{MAX}_{\text{global}}$ and found the signature is only evident in the AOGCM, providing evidence that the effect of MAX topography on global climate manifests through atmosphere–ocean coupling.

As the horizontal resolution of E2.1 is 5 times coarser than CM2.5-FLOR (2.5° vs 50 km , respectively), the application of $\text{MAX}_{\text{global}}$ in E2.1 led to approximately 5 times more land surface area at the highest observed elevations than in CM2.5-FLOR. This created unrealistically wide orographic features relative to observations, including an anomalously high-elevation plateau over the western United States. This plateau likely contributed to the AMOC slowdown in the E2.1 $\text{MAX}_{\text{global}}$ simulation (Fig. 12c) by altering stationary wave patterns (Fig. A3) and increasing friction that decelerated surface winds over the North Atlantic (Fig. A4). These results highlight how orography–atmosphere interactions can modulate AMOC strength via wind- and buoyancy-driven ocean currents and their impacts on heat transport, salinity, and mixing in the Atlantic basin (Nilsson et al. 2021). While previous work has demonstrated that the existence of orography in North America favors an AMOC (Seager et al. 2002; Sinha et al. 2012; Maffre et al. 2018), we find that too-much orographic blocking upstream of the Atlantic basin can critically reduce AMOC strength. In addition to the effect of model resolution on the extent of high topography with $\text{MAX}_{\text{global}}$, differences in the sensitivity of AMOC to atmospheric variations between the E2.1 and CM2.5-FLOR models may explain their contrasting responses to $\text{MAX}_{\text{global}}$ topography; model-specific parameterizations and horizontal resolution are known to contribute to the intermodel spread in the representation of AMOC in climate models (Roberts et al. 2020; Li et al. 2021).

Ultimately, topographic BCs composed of gridcell maximum topography, such as $\text{MAX}_{\text{global}}$, are likely inappropriate for coarse-resolution ($>2^\circ$) GCMs. To date, studies evaluating the efficacy of MAX topography in 1° models have only tested the topographic modification regionally (Baldwin et al. 2021; Xu and Lee 2021), so it is unclear how other climate models would respond to $\text{MAX}_{\text{global}}$. The community should exercise caution particularly when considering the application of MAX topography over orographic regions that have large widths in addition to their lengths (e.g., the western United States and Tibetan Plateau) as the modification can result in

unrealistically broad regions of elevated terrain that increase the time needed for air to flow across the barrier, generating a substantial planetary wave response (Li and Zhu 1990; Holton 1993; Lenters et al. 1995).

5. Conclusions

As covered in the introduction (section 1), it is well documented that the standard method for developing model-resolved surface height boundary conditions (i.e., taking the gridcell average of observed surface height) results in overly smooth topography that underestimates the flow-blocking capabilities of orography. How to ameliorate this bias is an ongoing debate. We explored the use of the Froude parameter F as an objective, dynamical framework for selecting the optimal model surface height boundary condition and found a nuanced answer as the response of circulation to topography is highly dependent on horizontal resolution. Though the use of gridcell maximum topography is an interesting sensitivity test that has shed light on the underestimation of orographic blocking in other models (Xu and Lee 2021; Baldwin et al. 2021), we found that when this methodology is applied to coarse-resolution model grids such as E2.1, it generates unrealistically large plateaus with very high elevations that impose dramatic perturbations to global climate (such as the shutdown of AMOC). For the E2.1 model with a $2^\circ \times 2.5^\circ$ horizontal resolution, an envelope interpolation scheme in which the 1σ variance of subgrid cell topography is added to the gridcell mean (Wallace et al. 1983) generates the most realistic pattern of orographic blocking, inferred from F , in Central and South America. The F framework would likely be helpful for selecting optimal model topography in other regions where the orientation of the mean zonal flow is orthogonal to orography, for example, the Western Ghats (cf. Xie et al. 2006; Phadtare et al. 2022).

Our experiments build upon prior work evaluating the role of topographic biases in Central and South America in coarse- and intermediate-resolution GCMs by expanding these analyses to a new model (E2.1) that employs unique physics schemes (Kelley et al. 2020) and also by modifying both these topographic features in concert. By assessing how our experiments with modified topography reduce existing model biases in E2.1 and the extent to which these patterns are consistent across our study and other studies employing different GCMs forced with elevated topography, we can ascribe the relative importance of mechanical processes associated with orography compared to other sources of model biases, such as model cloud physics schemes or atmosphere–ocean coupled processes.

We find that elevating the Central American Cordillera enhanced blocking of the northeasterlies and reduced near-surface wind speeds over the EPWP on the lee side of the range. In the experiment where only Central America was elevated (CA-ONLY), this reduces surface fluxes and increases SST in the EPWP, consistent with the results in Baldwin et al. (2021) concerning the impact of elevating Central American topography in the CM2.5-FLOR model. The increase in SST north of the equator in CA-ONLY strengthens the meridional

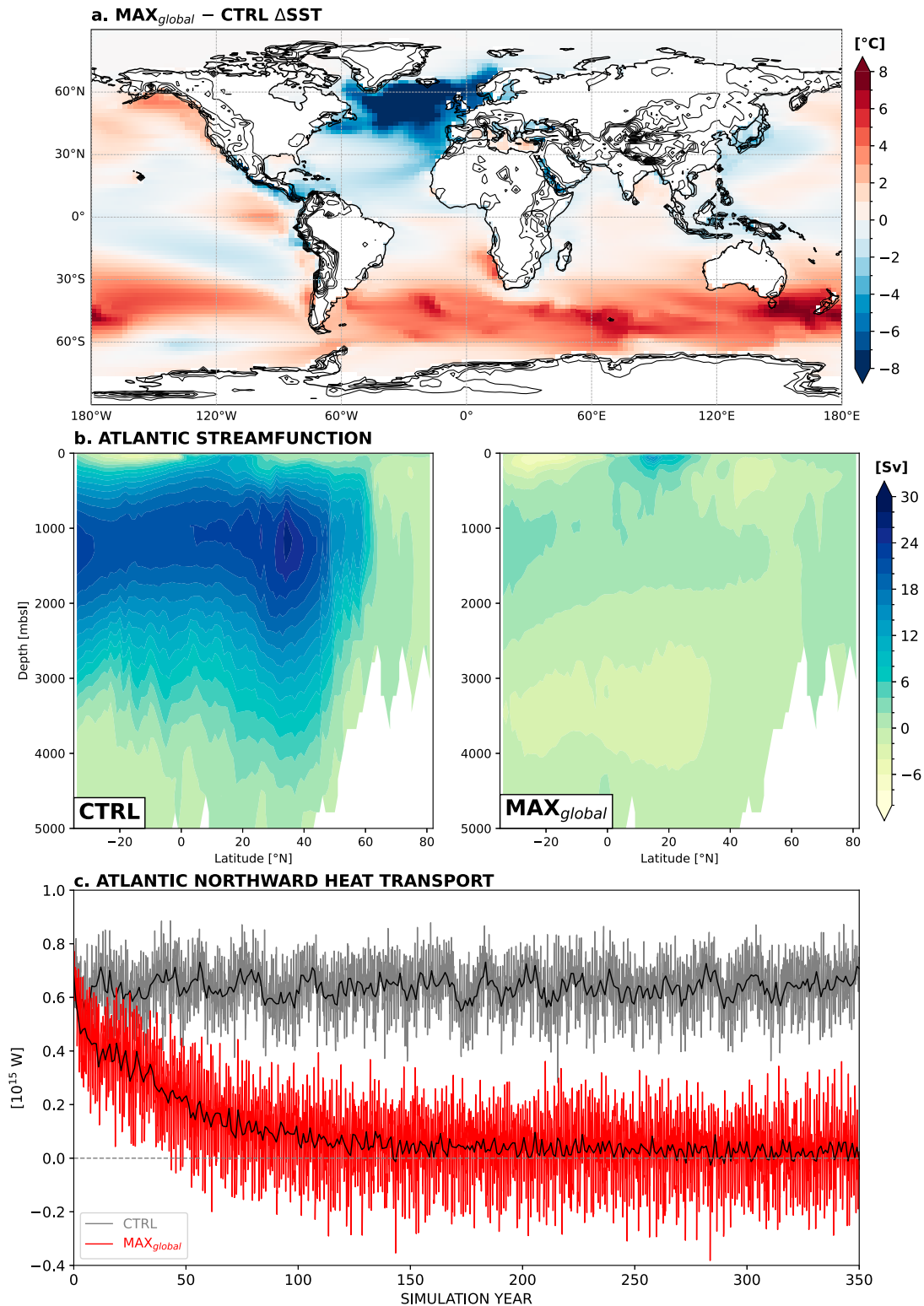


FIG. 12. Impact of the global application of MAX topography on SST and AMOC in E2.1. (a) Difference in mean annual SST (colored shading) and topography (black contours, for elevation >500 m with intervals of 500 m) in MAX_{global} relative to the AOGCM CTRL, (b) mean annual Atlantic streamfunction as an indicator of AMOC strength, and (c) time series of basin-mean northward heat transport in the Atlantic.

SST gradient in the eastern tropical Pacific and enhances low-level moisture flux convergence in the northeast Pacific ITCZ. These results demonstrate that increasing topography over Central America is effective for reducing model biases in the north-eastern tropical Pacific, including a slight improvement in the eastern Pacific double-ITCZ bias.

Increased topographic heights in the Andes in South America appear to shift circulation and SST in the subtropical South Pacific in E2.1 in a pattern more consistent with observations. The low-level circulation in the model responds predictably to the greater orographic blocking power of the elevated Andes by deflecting the westerly zonal flow equatorward and, consequently, strengthening the descent of dry air and the speed of the southeasterlies that decrease underlying SST through evaporative cooling. As in [Takahashi and Battisti \(2007a\)](#) and [Xu and Lee \(2021\)](#), this suppresses convection in the South Pacific and reduces the positive precipitation bias in the southeastern ITCZ. The enhanced anticyclonic circulation related to the higher Andes topography and associated SST cooling also strengthens the zonal SST gradient in the South Pacific. This leads to an improvement in the transport and convergence of tropical moisture in the SPCZ. Yet, due to spatial offsets between these shifts and the location of the strongest model biases in CTRL as well as the remote impact of the elevated topography on the climate of the Caribbean and north-central Pacific, there is marginal improvement in the overall RMSE of the low-level winds and SST fields in the CA+SA experiment.

Furthermore, though the higher Andes topography strengthens the low-level southeasterly winds and lowers SST in the southeast Pacific, these changes in regional circulation do not generate a substantial increase in the strength of the cross-equatorial southerly winds nor low-level (1000–850 hPa) moisture flux convergence and precipitation in the northeastern Pacific ITCZ. Rather, we actually observe an exacerbation of the dry bias at $\sim 10^{\circ}\text{N}$ after increasing the elevation of the Andes. The positive impact of elevating Central American topography alone on the double-ITCZ bias in E2.1, which is smaller than in [Baldwin et al. \(2021\)](#), is apparently overwhelmed by the effect of elevating the Andes; elevating Central and South American topography simultaneously thus resulted in no net improvement in the regional double ITCZ. It is possible that elevating the Andes has limited effects in CM2.5-FLOR relative to E2.1 because the high resolution (50 km) of CM2.5-FLOR may already allow sufficient resolution of the Andes' blocking ([Junquas et al. 2016](#)). This discrepancy could also be due to the fact that the coarse-resolution E2.1 model does not resolve the necessary wind-driven surface currents (i.e., the NECC) that provide an important feedback on ITCZ location and intensity north of the equator in the far eastern Pacific ([Sun and Lu 2021](#); [Baldwin et al. 2021](#)). The higher Andes in E2.1 may have also had a remote impact on EPWP SST by cooling the Caribbean air which flows into the EPWP, attenuating the effect of the enhanced orographic blocking by the Central American Cordillera on EPWP SST. Alternatively, we posit that the lack of increase in convergence and precipitation north of the equator despite improvements in circulation and SST biases in the South Pacific in response to the elevated Andes in the CA+SA

experiment may relate to radiation biases in E2.1 arising from the poor representation of subtropical stratocumulus clouds. Our results add to the wide body of literature underscoring the importance of cloud-radiative feedbacks on the Pacific double-ITCZ bias via extratropical–tropical interactions ([Philander et al. 1996](#); [Li and Xie 2014](#); [Xiang et al. 2018](#); [Kang et al. 2019](#)).

We find the impact of the various topographic modifications on near-surface moisture convergence best explains patterns of precipitation in our simulations. The effect of local SST on surface fluxes is of lesser importance. Understanding the effect of topographic and other model biases on regional SST gradients that drive convergence in the boundary layer is therefore paramount for reducing model precipitation biases in the basin, including the double ITCZ. A study from [Zhou et al. \(2020\)](#) analyzing Pacific ITCZ biases in CMIP5 and CMIP6 models found that patterns of near-surface convergence associated with biases in meridional SST gradients also explain the anomalous northward displacement of the ITCZ in the north-central Pacific. E2.1 exhibits a similar bias, yet we find that neither modifying Central or South American topography reduces the excess precipitation centered at $\sim 10^{\circ}\text{N}$ in the north-central Pacific due to the lack of improvement in the underlying SST gradient.

The aspects of our simulations that are robust and yet incongruous with prior studies investigating the impact of Central and South American topography on Pacific climate both raise exciting new questions to explore in future work. We hypothesize that the limited impact of modifying South American topography on the eastern equatorial Pacific climate in E2.1 is related to model cloud-radiative biases. As improvements to the simulation of stratocumulus clouds have been an area of focus in the development of the newest generation of GCMs (e.g., [Woelfle et al. 2019](#)), we can test this hypothesis by evaluating the robustness of the impact of topography on Pacific climate in models with reduced low cloud biases, such as E3 ([Cesana et al. 2019](#); [Elsaesser et al. 2025](#)). Though the horizontal resolution of E2.1 is on the lower end of the current generation of GCMs, our experiments are relevant for paleoclimate and future climate studies that still commonly utilize GCMs with 1° – 2° resolutions. Biases in the simulation of the Pacific climate currently hamper the utility of GCMs for understanding and projecting past, present, and future climate variability. Elevated topography in Central and South America can improve the simulation of interannual climate variability associated with the El Niño–Southern Oscillation (cf. [Xu and Lee 2021](#); [Baldwin et al. 2021](#)); however, its effect on the representation of lower frequency variability has yet to be explored. Atmosphere–ocean teleconnections in the Pacific are a pacemaker of global decadal climate variability, including the 1998–2013 hiatus in global mean surface warming ([Xie and Kosaka 2017](#)), though SST biases in GCMs lead to the near absence of the conditions necessary to simulate these feedbacks ([Seager et al. 2019](#); [Li et al. 2020](#)). The latest GCMs contributing to CMIP6 generally fail to reproduce the strengthening of the climatological SST gradients in the Pacific during the historical period ([Dong et al. 2022](#); [Seager et al. 2022](#); [Wills et al. 2022](#); [Heede and Fedorov 2023](#)), which additionally undermines confidence in the ability of GCMs to

simulate long-term climate trends. Our results show that increasing the height of the Andes strengthens the zonal SST gradient in the South Pacific and may enable models to more realistically capture the shift to La Niña-like mean state conditions in the basin in response to increased greenhouse gas forcing (Seager et al. 2019). Improvements to Pacific climatology due to elevated topography may thus inform models' simulation of internal variability and the response to external forcing, which has implications for the simulation of precipitation and temperature over land, climate sensitivity, and the climatologies of climate extremes such as heatwaves and tropical cyclones.

Acknowledgments. This work is supported by NASA NIP Grant 80NSSC21K1735 and National Science Foundation (NSF) Grant EAR-2316736 awarded to J.W.B. and NSF Grant AGS-2429287 subawarded to J.W.B. Computing resources for data analysis were provided by the NASA High-End Computing (HEC) Program through the NASA Center for Climate Simulation (NCCS) at the Goddard Space Flight Center. Additional contributions by G.S.E. were supported by the NASA Modeling, Analysis and Prediction Program and APAM-GISS Cooperative Agreement 80NSSC18M0133, as well as NASA Precipitation Measurement Missions Grant 80NSSC22K0609. We thank Reto Reudy and Maxwell Kelley at NASA GISS for their assistance with the E2.1 simulations.

Data availability statement. Data from the E2.1 simulations conducted as a part of this study and relevant observational

data from reanalysis and satellite products used to calculate model biases are available to download via the Zenodo repository (<https://zenodo.org/records/13941966>). Jupyter notebooks for figures are provided on D.M.K.'s GitHub (<https://github.com/dervlamk/E2.1-Topo-BCs>). ETOPO global relief data are freely available from the NGDC (<https://www.ncei.noaa.gov/products/etopo-global-relief-model>).

APPENDIX

Modified E2.1 Topographic Boundary Conditions and Their Impacts

In Fig. A1, we compare the grid-averaged surface heights for the five modified topographic BCs implemented in the E2.1 AGCM to the CTRL surface height.

Figure A2 compares the strength of the near-surface (16 m) zonal current in the northeastern Pacific to the gradient of wind stress curl in the CTRL and modified topography simulations conducted as part of this study and those from Baldwin et al. (2021).

Figures A3 and A4 are provided to better understand the mechanism(s) through which the impact of the MAX_{global} on atmospheric circulation could have led to the slowdown of the Atlantic meridional overturning circulation—either by altering stationary wave patterns (Fig. A3) or low-level wind speeds (Fig. A4).

Table A1 provides detailed information on the CMIP6 models used to construct the multimodel ensemble mean biases in Fig. 1.

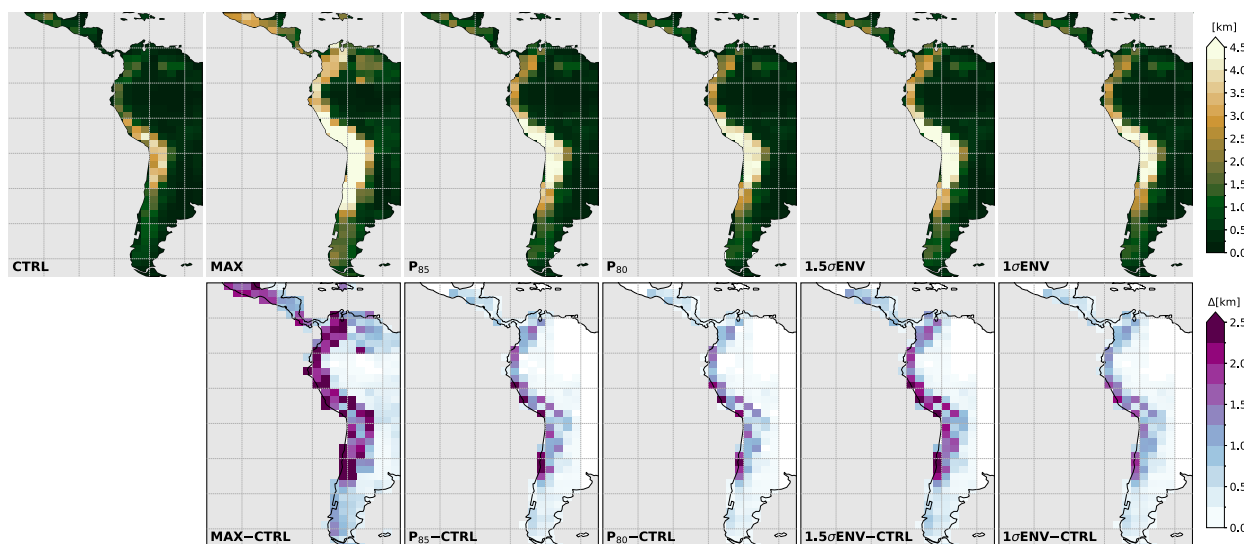


FIG. A1. (top) Topography corresponding to the CTRL and modified (MAX, P_{85} , P_{80} , $1.5\sigma ENV$, and $1\sigma ENV$) BCs, and (bottom) the difference in surface elevation between the modified BCs and CTRL.

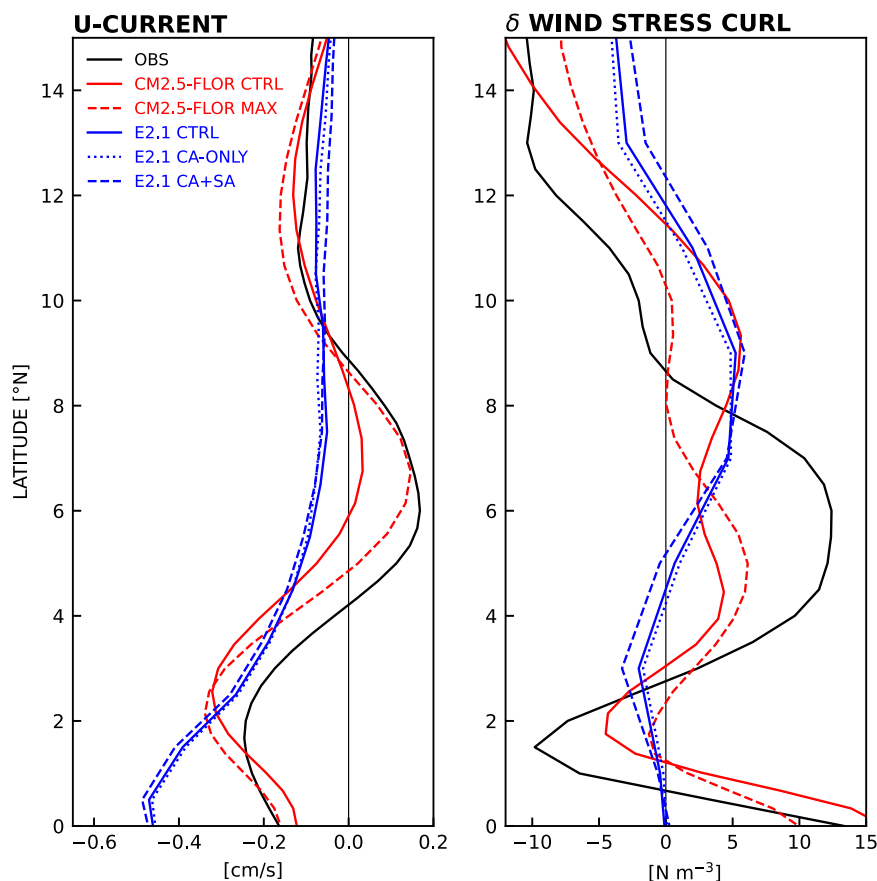


FIG. A2. Comparison of (left) northeastern Pacific east–west current strength and (right) the gradient of wind stress curl for observations (OSCAR), CM2.5-FLOR forced with CTRL and MAX topography, and E2.1 forced with CTRL and 1 σ ENV topography in CA-ONLY and CA+SA. Zonal-mean profiles calculated between 170° and 110°W.

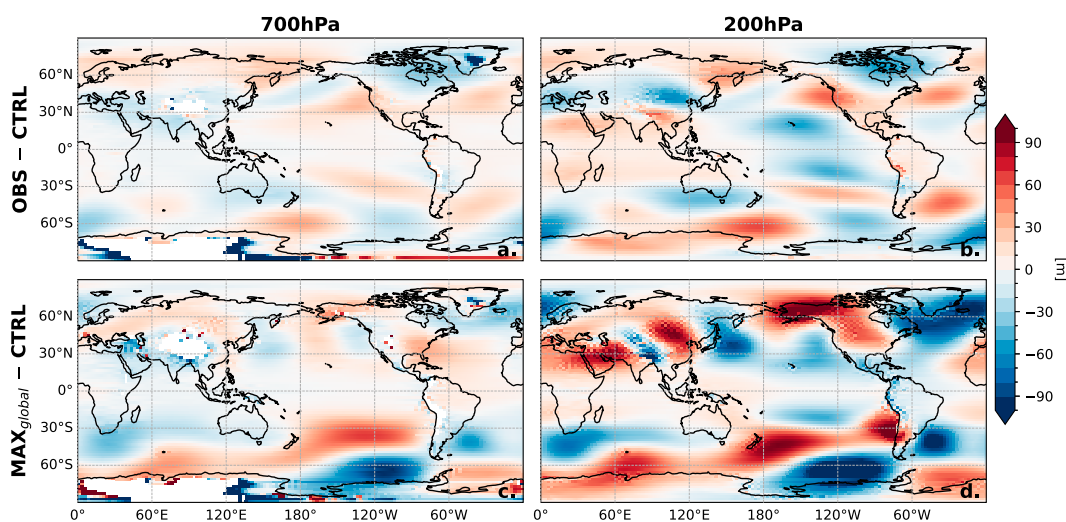


FIG. A3. Inverse of the E2.1 CTRL model bias of stationary wave patterns at (a) 700 and (b) 200 hPa, and the effect of MAX_{global} topography on the CTRL stationary wave bias at (c) 700 and (d) 200 hPa. Stationary wave patterns were calculated as the difference in atmospheric height at each gridcell relative to the time mean zonal mean.

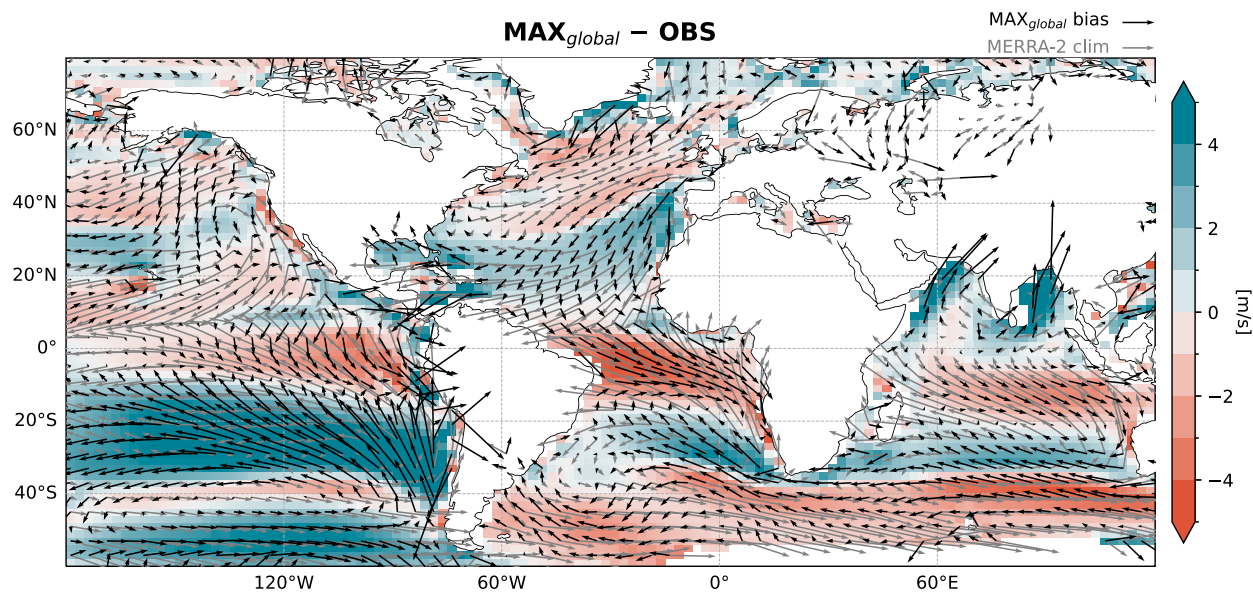


FIG. A4. MAX_{global} observation difference in mean annual 1000-hPa wind speed (shading) and direction (black vectors) highlighting the effect of MAX topography on E2.1 biases. Red (blue) colors show where the model is slower (faster) than observations. Wind speed and direction were calculated from U and V components. Gray vectors show observed climatological 1000-hPa wind from MERRA-2.

TABLE A1. CMIP6 model simulations used in Fig. 1.

Model	Precipitation	10-m wind speed	SST
ACCESS-CM2	✓	✓	✓
ACCESS-ESM1-5	✓	✓	✓
AWI-CM-1-1-MR	✓	✓	✓
AWI-ESM-1-1-LR	✓	✓	✓
BCC_CSM2-MR	✓	✓	✓
CAMS-CSM1-0	✓	✓	✓
CAS-ESM2-0	✓	✓	✓
CESM2	✓		✓
CESM2-FV2	✓		✓
CESM2(WACCM)	✓		✓
CESM2(WACCM)-FV2	✓		✓
CIESM			✓
CMCC-CM2-HR4	✓	✓	✓
CMCC-CM2-SR5	✓	✓	✓
CMCC-ESM2	✓	✓	✓
E3SM-1-0	✓		✓
E3SM-1-1	✓		✓
E3SM-1-1-ECA	✓		✓
EC-EARTH3	✓	✓	✓
EC-EARTH3-AerChem	✓	✓	✓
EC-EARTH3-CC	✓	✓	✓
EC-EARTH3-Veg	✓	✓	✓
EC-EARTH3-Veg-LR	✓	✓	✓
FGOALS-f3-L	✓	✓	✓
FIO-ESM-2-0	✓	✓	✓
GFDL-CM4	✓	✓	✓
GFDL-ESM4	✓	✓	✓
GISS-E2-1-G	✓	✓	✓
GISS-E2-1-G-CC	✓	✓	✓
GISS-E2-1-H	✓	✓	✓
GISS-E2-2-H	✓		✓
IITM-ESM	✓	✓	✓
INM-CM4-8	✓	✓	✓
INM-CM5-0	✓	✓	✓
IPSL-CM5A2-INCA	✓	✓	✓
IPSL-CM6A-LR	✓	✓	✓
IPSL-CM6A-LR-INCA	✓	✓	✓
KACE-1-0-G	✓	✓	✓
KIOST-ESM	✓	✓	✓
MIROC6	✓	✓	✓
MPI-ESM-1-2-HAM	✓	✓	✓
MPI-ESM1-2-HR	✓	✓	✓
MPI-ESM1-2-LR	✓	✓	✓
MRI-ESM2-0	✓	✓	✓
NESM3	✓	✓	✓
NorCPM1	✓	✓	✓
NorESM2-LM	✓		✓
NorESM2-MM	✓		✓
SAM0-UNICON	✓		✓
TaiESM1	✓		✓

REFERENCES

- Amador, J. A., E. J. Alfaro, O. G. Lizano, and V. O. Magaña, 2006: Atmospheric forcing of the eastern tropical Pacific: A review. *Prog. Oceanogr.*, **69**, 101–142, <https://doi.org/10.1016/j.pocean.2006.03.007>.
- Back, L. E., and C. S. Bretherton, 2009a: A simple model of climatological rainfall and vertical motion patterns over the tropical oceans. *J. Climate*, **22**, 6477–6497, <https://doi.org/10.1175/2009JCLI2393.1>.
- , and —, 2009b: On the relationship between SST gradients, boundary layer winds, and convergence over the tropical oceans. *J. Climate*, **22**, 4182–4196, <https://doi.org/10.1175/2009JCLI2392.1>.
- Baines, P. G., and R. B. Smith, 1993: Upstream stagnation points in stratified flow past obstacles. *Dyn. Atmos. Oceans*, **18**, 105–113, [https://doi.org/10.1016/0377-0265\(93\)90005-R](https://doi.org/10.1016/0377-0265(93)90005-R).
- Baldwin, J. W., A. R. Atwood, G. A. Vecchi, and D. S. Battisti, 2021: Outsize influence of Central American orography on global climate. *AGU Adv.*, **2**, e2020AV000343, <https://doi.org/10.1029/2020AV000343>.
- Battisti, D. S., E. S. Sarachik, and A. C. Hirst, 1999: A consistent model for the large-scale steady surface atmospheric circulation in the tropics. *J. Climate*, **12**, 2956–2964, [https://doi.org/10.1175/1520-0442\(1999\)012<2956:ACMFTL>2.0.CO;2](https://doi.org/10.1175/1520-0442(1999)012<2956:ACMFTL>2.0.CO;2).
- Bauer, M. H., G. J. Mayr, I. Vergeiner, and H. Pichler, 2000: Strongly nonlinear flow over and around a three-dimensional mountain as a function of the horizontal aspect ratio. *J. Atmos. Sci.*, **57**, 3971–3991, [https://doi.org/10.1175/1520-0469\(2001\)058<3971:SNFOAA>2.0.CO;2](https://doi.org/10.1175/1520-0469(2001)058<3971:SNFOAA>2.0.CO;2).
- Bony, S., and J.-L. Dufresne, 2005: Marine boundary layer clouds at the heart of tropical cloud feedback uncertainties in climate models. *Geophys. Res. Lett.*, **32**, L20806, <https://doi.org/10.1029/2005GL023851>.
- Brown, J. R., and Coauthors, 2020: South Pacific Convergence Zone dynamics, variability and impacts in a changing climate. *Nat. Rev. Earth Environ.*, **1**, 530–543, <https://doi.org/10.1038/s43017-020-0078-2>.
- Cai, W., and Coauthors, 2019: Pantropical climate interactions. *Science*, **363**, eaav4236, <https://doi.org/10.1126/science.aav4236>.
- Cesana, G., A. D. Del Genio, A. S. Ackerman, M. Kelley, G. Elsaesser, A. M. Fridlind, Y. Cheng, and M.-S. Yao, 2019: Evaluating models' response of tropical low clouds to SST forcings using CALIPSO observations. *Atmos. Chem. Phys.*, **19**, 2813–2832, <https://doi.org/10.5194/acp-19-2813-2019>.
- Chiang, J. C. H., and A. R. Friedman, 2012: Extratropical cooling, interhemispheric thermal gradients, and tropical climate change. *Annu. Rev. Earth Planet. Sci.*, **40**, 383–412, <https://doi.org/10.1146/annurev-earth-042711-105545>.
- , S. E. Zebiak, and M. A. Cane, 2001: Relative roles of elevated heating and surface temperature gradients in driving anomalous surface winds over tropical oceans. *J. Atmos. Sci.*, **58**, 1371–1394, [https://doi.org/10.1175/1520-0469\(2001\)058<1371:RROEHA>2.0.CO;2](https://doi.org/10.1175/1520-0469(2001)058<1371:RROEHA>2.0.CO;2).
- da Silveira, I. P., P. Zuidema, and B. P. Kirtman, 2019: Fast SST error growth in the southeast Pacific Ocean: Comparison between high and low-resolution CCSM4 retrospective forecasts. *Climate Dyn.*, **53**, 5237–5251, <https://doi.org/10.1007/s00382-019-04855-5>.
- De Szoeke, S. P., and S.-P. Xie, 2008: The tropical eastern Pacific seasonal cycle: Assessment of errors and mechanisms in IPCC AR4 coupled ocean–atmosphere general circulation models. *J. Climate*, **21**, 2573–2590, <https://doi.org/10.1175/2007JCLI1975.1>.
- Dong, Y., K. C. Armour, D. S. Battisti, and E. Blanchard-Wrigglesworth, 2022: Two-way teleconnections between the Southern Ocean and the tropical Pacific via a dynamic feedback. *J. Climate*, **35**, 6267–6282, <https://doi.org/10.1175/JCLI-D-22-0080.1>.
- Elsaesser, G., and Coauthors, 2025: Using machine learning to generate a GISS ModelE Calibrated Physics Ensemble (CPE).

- J. Adv. Model. Earth Syst.*, **17**, e2024MS004713, <https://doi.org/10.1029/2024MS004713>.
- Elvidge, A. D., and Coauthors, 2019: Uncertainty in the representation of orography in weather and climate models and implications for parameterized drag. *J. Adv. Model. Earth Syst.*, **11**, 2567–2585, <https://doi.org/10.1029/2019MS001661>.
- Espinoza, J. C., R. Garreaud, G. Poveda, P. A. Arias, J. Molina-Carpio, M. Masiokas, M. Viale, and L. Scaff, 2020: Hydroclimate of the Andes part I: Main climatic features. *Front. Earth Sci.*, **8**, 64, <https://doi.org/10.3389/feart.2020.00064>.
- Fu, D., P. Chang, C. M. Patricola, R. Saravanan, X. Liu, and H. E. Beck, 2021: Central American mountains inhibit eastern North Pacific seasonal tropical cyclone activity. *Nat. Commun.*, **12**, 4422, <https://doi.org/10.1038/s41467-021-24657-w>.
- Fu, R., A. D. Del Genio, and W. B. Rossow, 1994: Influence of ocean surface conditions on atmospheric vertical thermodynamic structure and deep convection. *J. Climate*, **7**, 1092–1108, [https://doi.org/10.1175/1520-0442\(1994\)007<1092:IOOSCO>2.0.CO;2](https://doi.org/10.1175/1520-0442(1994)007<1092:IOOSCO>2.0.CO;2).
- Galewsky, J., 2009: Rain shadow development during the growth of mountain ranges: An atmospheric dynamics perspective. *J. Geophys. Res.*, **114**, F01018, <https://doi.org/10.1029/2008JF001085>.
- , and A. Sobel, 2005: Moist dynamics and orographic precipitation in northern and central California during the New Year's flood of 1997. *Mon. Wea. Rev.*, **133**, 1594–1612, <https://doi.org/10.1175/MWR2943.1>.
- Gelaro, R., and Coauthors, 2017: The Modern-Era Retrospective Analysis for Research and Applications, version 2 (MERRA-2). *J. Climate*, **30**, 5419–5454, <https://doi.org/10.1175/JCLI-D-16-0758.1>.
- Ham, Y.-G., J.-S. Kug, J.-Y. Park, and F.-F. Jin, 2013: Sea surface temperature in the north tropical Atlantic as a trigger for El Niño/Southern Oscillation events. *Nat. Geosci.*, **6**, 112–116, <https://doi.org/10.1038/geo1686>.
- Heede, U. K., and A. V. Fedorov, 2023: Colder eastern equatorial Pacific and stronger walker circulation in the early 21st century: Separating the forced response to global warming from natural variability. *Geophys. Res. Lett.*, **50**, e2022GL101020, <https://doi.org/10.1029/2022GL101020>.
- Holton, J. R., 1993: The second Haurwitz memorial lecture: Stationary planetary waves. *Bull. Amer. Meteor. Soc.*, **74**, 1735–1742, <https://doi.org/10.1175/1520-0477-74.9.1735>.
- Huffman, G. J., D. T. Bolvin, E. J. Nelkin, and J. Tan, 2015: Integrated Multi-satellite Retrievals for GPM (IMERG) technical documentation. NASA/GSFC Code 612 Tech. Doc., 54 pp., https://gpm.nasa.gov/sites/default/files/document_files/IMERG_doc.pdf.
- Insel, N., C. J. Poulsen, and T. A. Ehlers, 2010: Influence of the Andes Mountains on South American moisture transport, convection, and precipitation. *Climate Dyn.*, **35**, 1477–1492, <https://doi.org/10.1007/s00382-009-0637-1>.
- Jarraud, M., A. J. Simmons, and M. Kanamitsu, 1988: Sensitivity of medium-range weather forecasts to the use of an envelope orography. *Quart. J. Roy. Meteor. Soc.*, **114**, 989–1025, <https://doi.org/10.1002/qj.49711448208>.
- Jiang, L., and T. Li, 2021: Impacts of tropical North Atlantic and equatorial Atlantic SST anomalies on ENSO. *J. Climate*, **34**, 5635–5655, <https://doi.org/10.1175/JCLI-D-20-0835.1>.
- Jiang, Q., 2003: Moist dynamics and orographic precipitation. *Tellus*, **55A**, 301–316, <https://doi.org/10.1034/j.1600-0870.2003.00025.x>.
- Junquas, C., L. Li, C. S. Vera, H. L. Treut, and K. Takahashi, 2016: Influence of South America orography on summertime precipitation in Southeastern South America. *Climate Dyn.*, **46**, 3941–3963, <https://doi.org/10.1007/s00382-015-2814-8>.
- Kang, S. M., and Coauthors, 2019: Extratropical–Tropical Interaction Model Intercomparison Project (ETIN-MIP): Protocol and initial results. *Bull. Amer. Meteor. Soc.*, **100**, 2589–2606, <https://doi.org/10.1175/BAMS-D-18-0301.1>.
- Kelley, M., and Coauthors, 2020: GISS-E2.1: Configurations and climatology. *J. Adv. Model. Earth Syst.*, **12**, e2019MS002025, <https://doi.org/10.1029/2019MS002025>.
- Kessler, W. S., 2006: The circulation of the eastern tropical Pacific: A review. *Prog. Oceanogr.*, **69**, 181–217, <https://doi.org/10.1016/j.pocean.2006.03.009>.
- Kim, H., S. M. Kang, J. E. Kay, and S.-P. Xie, 2022: Subtropical clouds key to Southern Ocean teleconnections to the tropical Pacific. *Proc. Natl. Acad. Sci. USA*, **119**, e2200514119, <https://doi.org/10.1073/pnas.2200514119>.
- Lauritzen, P. H., J. T. Bacmeister, P. F. Callaghan, and M. A. Taylor, 2015: NCAR_Topo (v1.0): NCAR global model topography generation software for unstructured grids. *Geosci. Model Dev.*, **8**, 3975–3986, <https://doi.org/10.5194/gmd-8-3975-2015>.
- Lenters, J. D., K. H. Cook, and T. D. Ringler, 1995: Comments on “On the influence of the Andes on the general circulation of the Southern Hemisphere”. *J. Climate*, **8**, 2113–2115, [https://doi.org/10.1175/1520-0442\(1995\)008<2113:COTIOT>2.0.CO;2](https://doi.org/10.1175/1520-0442(1995)008<2113:COTIOT>2.0.CO;2).
- Li, C., D. Dommenges, and S. McGregor, 2020: Trans-basin Atlantic-Pacific connections further weakened by common model Pacific mean SST biases. *Nat. Commun.*, **11**, 5677, <https://doi.org/10.1038/s41467-020-19338-z>.
- Li, G., and S.-P. Xie, 2014: Tropical biases in CMIP5 multimodel ensemble: The excessive equatorial Pacific cold tongue and double ITCZ problems. *J. Climate*, **27**, 1765–1780, <https://doi.org/10.1175/JCLI-D-13-00337.1>.
- Li, H., A. Fedorov, and W. Liu, 2021: AMOC stability and diverging response to Arctic sea ice decline in two climate models. *J. Climate*, **34**, 5443–5460, <https://doi.org/10.1175/JCLI-D-20-0572.1>.
- Li, L., and B. Zhu, 1990: The modified envelope orography and the air flow over and around mountains. *Adv. Atmos. Sci.*, **7**, 249–260, <https://doi.org/10.1007/BF03179759>.
- Lindzen, R. S., and S. Nigam, 1987: On the role of sea surface temperature gradients in forcing low-level winds and convergence in the tropics. *J. Atmos. Sci.*, **44**, 2418–2436, [https://doi.org/10.1175/1520-0469\(1987\)044<2418:OTROSS>2.0.CO;2](https://doi.org/10.1175/1520-0469(1987)044<2418:OTROSS>2.0.CO;2).
- Liu, T., Z. Liu, Y. Zhao, and S. Zhang, 2023: Subtropical impact on the tropical double-ITCZ Bias in the GFDL CM2.1 model. *J. Climate*, **36**, 3833–3847, <https://doi.org/10.1175/JCLI-D-22-0432.1>.
- Loeb, N. G., and Coauthors, 2018: Clouds and the Earth's Radiant Energy System (CERES) Energy Balanced and Filled (EBAF) Top-of-Atmosphere (TOA) edition-4.0 data product. *J. Climate*, **31**, 895–918, <https://doi.org/10.1175/JCLI-D-17-0208.1>.
- Lott, F., and M. J. Miller, 1997: A new subgrid-scale orographic drag parametrization: Its formulation and testing. *Quart. J. Roy. Meteor. Soc.*, **123**, 101–127, <https://doi.org/10.1002/qj.49712353704>.
- Maffre, P., J.-B. Ladant, Y. Donnadieu, P. Sepulchre, and Y. Godd  ris, 2018: The influence of orography on modern ocean circulation. *Climate Dyn.*, **50**, 1277–1289, <https://doi.org/10.1007/s00382-017-3683-0>.

- Mass, C. F., and G. K. Ferber, 1990: Surface pressure perturbations produced by an isolated mesoscale topographic barrier. Part I: General characteristics and dynamics. *Mon. Wea. Rev.*, **118**, 2579–2596, [https://doi.org/10.1175/1520-0493\(1990\)118<2579:SPPBA>2.0.CO;2](https://doi.org/10.1175/1520-0493(1990)118<2579:SPPBA>2.0.CO;2).
- Miller, M. J., T. N. Palmer, and R. Swinbank, 1989: Parametrization and influence of subgridscale orography in general circulation and numerical weather prediction models. *Meteor. Atmos. Phys.*, **40**, 84–109, <https://doi.org/10.1007/BF01027469>.
- Miller, R. L., and Coauthors, 2021: CMIP6 historical simulations (1850–2014) with GISS-E2.1. *J. Adv. Model. Earth Syst.*, **13**, e2019MS002034, <https://doi.org/10.1029/2019MS002034>.
- Myers, T. A., and J. R. Norris, 2013: Observational evidence that enhanced subsidence reduces subtropical marine boundary layer cloudiness. *J. Climate*, **26**, 7507–7524, <https://doi.org/10.1175/JCLI-D-12-00736.1>.
- National Geophysical Data Center, 1993: 5-minute Gridded Global Relief Data (ETOPO5). National Geophysical Data Center, NOAA, accessed 19 October 2022, <https://doi.org/10.7289/V5D798BF>.
- , 2006: 2-minute gridded global relief data (ETOPO2) v2. National Geophysical Data Center, NOAA, <https://doi.org/10.7289/V5J1012Q>.
- Naumann, A. K., B. Stevens, and C. Hohenegger, 2019: A moist conceptual model for the boundary layer structure and radiatively driven shallow circulations in the trades. *J. Atmos. Sci.*, **76**, 1289–1306, <https://doi.org/10.1175/JAS-D-18-0226.1>.
- Nilsson, J., D. Ferreira, T. Schneider, and R. C. J. Wills, 2021: Is the surface salinity difference between the Atlantic and Indo-Pacific a signature of the Atlantic meridional overturning circulation? *J. Phys. Oceanogr.*, **51**, 769–787, <https://doi.org/10.1175/JPO-D-20-0126.1>.
- Oueslati, B., and G. Bellon, 2013: Tropical precipitation regimes and mechanisms of regime transitions: Contrasting two aquaplanet general circulation models. *Climate Dyn.*, **40**, 2345–2358, <https://doi.org/10.1007/s00382-012-1344-x>.
- Palmer, T. N., G. J. Shutts, and R. Swinbank, 1986: Alleviation of a systematic westerly bias in general circulation and numerical weather prediction models through an orographic gravity wave drag parametrization. *Quart. J. Roy. Meteor. Soc.*, **112**, 1001–1039, <https://doi.org/10.1256/smsqj.47405>.
- Phadtare, J. A., J. K. Fletcher, A. N. Ross, A. G. Turner, and R. K. H. Schiemann, 2022: Froude-number-based rainfall regimes over the Western Ghats mountains of India. *Quart. J. Roy. Meteor. Soc.*, **148**, 3388–3405, <https://doi.org/10.1002/qj.4367>.
- Philander, S. G. H., D. Gu, G. Lambert, T. Li, D. Halpern, N.-C. Lau, and R. C. Pacanowski, 1996: Why the ITCZ is mostly north of the equator. *J. Climate*, **9**, 2958–2972, [https://doi.org/10.1175/1520-0442\(1996\)009<2958:WTIMN>2.0.CO;2](https://doi.org/10.1175/1520-0442(1996)009<2958:WTIMN>2.0.CO;2).
- Pierrehumbert, R. T., and B. Wyman, 1985: Upstream effects of mesoscale mountains. *J. Atmos. Sci.*, **42**, 977–1003, [https://doi.org/10.1175/1520-0469\(1985\)042<0977:UEOMM>2.0.CO;2](https://doi.org/10.1175/1520-0469(1985)042<0977:UEOMM>2.0.CO;2).
- Popp, M., and L. G. Silvers, 2017: Double and single ITCZs with and without clouds. *J. Climate*, **30**, 9147–9166, <https://doi.org/10.1175/JCLI-D-17-0062.1>.
- Raymond, D. J., G. B. Raga, C. S. Bretherton, J. Molinari, C. López-Carrillo, and Ž. Fuchs, 2003: Convective forcing in the intertropical convergence zone of the eastern Pacific. *J. Atmos. Sci.*, **60**, 2064–2082, [https://doi.org/10.1175/1520-0469\(2003\)060<2064:CFITIC>2.0.CO;2](https://doi.org/10.1175/1520-0469(2003)060<2064:CFITIC>2.0.CO;2).
- , C. S. Bretherton, and J. Molinari, 2006: Dynamics of the intertropical convergence zone of the east Pacific. *J. Atmos. Sci.*, **63**, 582–597, <https://doi.org/10.1175/JAS3642.1>.
- Rayner, N. A., D. E. Parker, E. B. Horton, C. K. Folland, L. V. Alexander, D. P. Rowell, E. C. Kent, and A. Kaplan, 2003: Global analyses of sea surface temperature, sea ice, and night marine air temperature since the late nineteenth century. *J. Geophys. Res.*, **108**, 4407, <https://doi.org/10.1029/2002JD002670>.
- Remote Sensing Systems, 2016: Monthly Mean Wind Speed Data Set on a 1 degree grid made from Remote Sensing Systems Version-7 Microwave Radiometer Data, V0701. www.remss.com.
- Roberts, M. J., and Coauthors, 2020: Sensitivity of the Atlantic Meridional Overturning Circulation to model resolution in CMIP6 HighResMIP simulations and implications for future changes. *J. Adv. Model. Earth Syst.*, **12**, e2019MS002014, <https://doi.org/10.1029/2019MS002014>.
- Rodwell, M. J., and B. J. Hoskins, 2001: Subtropical anticyclones and summer monsoons. *J. Climate*, **14**, 3192–3211, [https://doi.org/10.1175/1520-0442\(2001\)014<3192:SAASM>2.0.CO;2](https://doi.org/10.1175/1520-0442(2001)014<3192:SAASM>2.0.CO;2).
- Sandu, I., P. Bechtold, A. Beljaars, A. Bozzo, F. Pithan, T. G. Shepherd, and A. Zadra, 2016: Impacts of parameterized orographic drag on the Northern Hemisphere winter circulation. *J. Adv. Model. Earth Syst.*, **8**, 196–211, <https://doi.org/10.1002/2015MS000564>.
- , and Coauthors, 2019: Impacts of orography on large-scale atmospheric circulation. *npj Climate Atmos. Sci.*, **2**, 10, <https://doi.org/10.1038/s41612-019-0065-9>.
- Seager, R., D. S. Battisti, J. Yin, N. Gordon, N. Naik, A. C. Clement, and M. A. Cane, 2002: Is the Gulf Stream responsible for Europe's mild winters? *Quart. J. Roy. Meteor. Soc.*, **128**, 2563–2586, <https://doi.org/10.1256/qj.01.128>.
- , M. Cane, N. Henderson, D.-E. Lee, R. Abernathey, and H. Zhang, 2019: Strengthening tropical Pacific zonal sea surface temperature gradient consistent with rising greenhouse gases. *Nat. Climate Change*, **9**, 517–522, <https://doi.org/10.1038/s41558-019-0505-x>.
- , N. Henderson, and M. Cane, 2022: Persistent discrepancies between observed and modeled trends in the tropical Pacific Ocean. *J. Climate*, **35**, 4571–4584, <https://doi.org/10.1175/JCLI-D-21-0648.1>.
- SeaPAC, 2013: QuikSCAT Level 2B Ocean Wind Vectors in 12.5km Slice Composites version 3. NASA Physical Oceanography Distributed Active Archive Center, accessed 11 July 2019, <https://doi.org/10.5067/QSX12-L2B01>.
- Seo, J., S. M. Kang, and D. M. W. Frierson, 2014: Sensitivity of intertropical convergence zone movement to the latitudinal position of thermal forcing. *J. Climate*, **27**, 3035–3042, <https://doi.org/10.1175/JCLI-D-13-00691.1>.
- Sinha, B., A. T. Blaker, J. J.-M. Hirschi, S. Bonham, M. Brand, S. Josey, R. S. Smith, and J. Marotzke, 2012: Mountain ranges favour vigorous Atlantic meridional overturning. *Geophys. Res. Lett.*, **39**, L02705, <https://doi.org/10.1029/2011GL050485>.
- Smith, R. B., 1989: Mountain-induced stagnation points in hydrostatic flow. *Tellus*, **41A**, 270–274, <https://doi.org/10.1111/j.1600-0870.1989.tb00381.x>.
- Song, F., and G. J. Zhang, 2017: Impact of tropical SSTs in the North Atlantic and southeastern Pacific on the eastern Pacific ITCZ. *J. Climate*, **30**, 1291–1305, <https://doi.org/10.1175/JCLI-D-16-0310.1>.
- Song, X., and G. J. Zhang, 2019: Culprit of the eastern Pacific double-ITCZ bias in the NCAR CESM1.2. *J. Climate*, **32**, 6349–6364, <https://doi.org/10.1175/JCLI-D-18-0580.1>.
- Straub, K. H., and G. N. Kiladis, 2002: Observations of a convectively coupled Kelvin wave in the eastern Pacific ITCZ.

- J. Atmos. Sci.*, **59**, 30–53, [https://doi.org/10.1175/1520-0469\(2002\)059<0030:OOACCK>2.0.CO;2](https://doi.org/10.1175/1520-0469(2002)059<0030:OOACCK>2.0.CO;2).
- Sun, Z., and J. Lu, 2021: The North Equatorial Countercurrent and the zonality of the Intertropical Convergence Zone. *Geophys. Res. Lett.*, **48**, e2021GL095657, <https://doi.org/10.1029/2021GL095657>.
- Takahashi, K., and D. S. Battisti, 2007a: Processes controlling the mean tropical Pacific precipitation pattern. Part I: The Andes and the eastern Pacific ITCZ. *J. Climate*, **20**, 3434–3451, <https://doi.org/10.1175/JCLI4198.1>.
- , and —, 2007b: Processes controlling the mean tropical Pacific precipitation pattern. Part II: The SPCZ and the southeast Pacific dry zone. *J. Climate*, **20**, 5696–5706, <https://doi.org/10.1175/2007JCLI1656.1>.
- Tian, B., and X. Dong, 2020: The double-ITCZ bias in CMIP3, CMIP5, and CMIP6 models based on annual mean precipitation. *Geophys. Res. Lett.*, **47**, e2020GL087232, <https://doi.org/10.1029/2020GL087232>.
- Tibaldi, S., 1986: Envelope orography and maintenance of the quasi-stationary circulation in the ECMWF global models. *Advances in Geophysics*, Vol. 29, Academic Press, 339–374, [https://doi.org/10.1016/S0065-2687\(08\)60045-X](https://doi.org/10.1016/S0065-2687(08)60045-X).
- Timmermann, A., and Coauthors, 2007: The influence of a weakening of the Atlantic meridional overturning circulation on ENSO. *J. Climate*, **20**, 4899–4919, <https://doi.org/10.1175/JCLI4283.1>.
- Toma, V. E., and P. J. Webster, 2010: Oscillations of the inter-tropical convergence zone and the genesis of easterly waves. Part I: Diagnostics and theory. *Climate Dyn.*, **34**, 587–604, <https://doi.org/10.1007/s00382-009-0584-x>.
- van der Wiel, K., A. J. Matthews, M. M. Joshi, and D. P. Stevens, 2016: Why the South Pacific Convergence Zone is diagonal. *Climate Dyn.*, **46**, 1683–1698, <https://doi.org/10.1007/s00382-015-2668-0>.
- van Niekerk, A., I. Sandu, and S. B. Vosper, 2018: The circulation response to resolved versus parametrized orographic drag over complex mountain terrains. *J. Adv. Model. Earth Syst.*, **10**, 2527–2547, <https://doi.org/10.1029/2018MS001417>.
- , and Coauthors, 2020: Constraining Orographic Drag Effects (COORDE): A model comparison of resolved and parametrized orographic drag. *J. Adv. Model. Earth Syst.*, **12**, e2020MS002160, <https://doi.org/10.1029/2020MS002160>.
- Vosper, S. B., A. R. Brown, and S. Webster, 2016: Orographic drag on islands in the NWP mountain grey zone. *Quart. J. Roy. Meteor. Soc.*, **142**, 3128–3137, <https://doi.org/10.1002/qj.2894>.
- , A. van Niekerk, A. Elvidge, I. Sandu, and A. Beljaars, 2020: What can we learn about orographic drag parametrisation from high-resolution models? A case study over the Rocky Mountains. *Quart. J. Roy. Meteor. Soc.*, **146**, 979–995, <https://doi.org/10.1002/qj.3720>.
- Wallace, J. M., S. Tibaldi, and A. J. Simmons, 1983: Reduction of systematic forecast errors in the ECMWF model through the introduction of an envelope orography. *Quart. J. Roy. Meteor. Soc.*, **109**, 683–717, <https://doi.org/10.1002/qj.49710946202>.
- , T. P. Mitchell, and C. Deser, 1989: The influence of sea-surface temperature on surface wind in the eastern equatorial Pacific: Seasonal and interannual variability. *J. Climate*, **2**, 1492–1499, [https://doi.org/10.1175/1520-0442\(1989\)002<1492:TIOST>2.0.CO;2](https://doi.org/10.1175/1520-0442(1989)002<1492:TIOST>2.0.CO;2).
- Wang, Y., S.-P. Xie, H. Xu, and B. Wang, 2004: Regional model simulations of marine boundary layer clouds over the south-east Pacific off South America. Part I: Control experiment. *Mon. Wea. Rev.*, **132**, 274–296, [https://doi.org/10.1175/1520-0493\(2004\)132<0274:RMSOMB>2.0.CO;2](https://doi.org/10.1175/1520-0493(2004)132<0274:RMSOMB>2.0.CO;2).
- , —, B. Wang, and H. Xu, 2005: Large-scale atmospheric forcing by southeast Pacific boundary layer clouds: A regional model study. *J. Climate*, **18**, 934–951, <https://doi.org/10.1175/JCLI3302.1>.
- White, R. H., J. M. Wallace, and D. S. Battisti, 2021: Revisiting the role of mountains in the Northern Hemisphere winter atmospheric circulation. *J. Atmos. Sci.*, **78**, 2221–2235, <https://doi.org/10.1175/JAS-D-20-0300.1>.
- Wills, R. C. J., Y. Dong, C. Proistosescu, K. C. Armour, and D. S. Battisti, 2022: Systematic climate model biases in the large-scale patterns of recent sea-surface temperature and sea-level pressure change. *Geophys. Res. Lett.*, **49**, e2022GL100011, <https://doi.org/10.1029/2022GL100011>.
- Woelfle, M. D., C. S. Bretherton, C. Hannay, and R. Neale, 2019: Evolution of the double-ITCZ bias through CESM2 development. *J. Adv. Model. Earth Syst.*, **11**, 1873–1893, <https://doi.org/10.1029/2019MS001647>.
- Xiang, B., M. Zhao, I. M. Held, and J.-C. Golaz, 2017: Predicting the severity of spurious “double ITCZ” problem in CMIP5 coupled models from AMIP simulations. *Geophys. Res. Lett.*, **44**, 1520–1527, <https://doi.org/10.1002/2016GL071992>.
- , —, Y. Ming, W. Yu, and S. M. Kang, 2018: Contrasting impacts of radiative forcing in the Southern Ocean versus southern tropics on ITCZ position and energy transport in one GFDL climate model. *J. Climate*, **31**, 5609–5628, <https://doi.org/10.1175/JCLI-D-17-0566.1>.
- Xie, S.-P., 2004: The shape of continents, air-sea interaction, and the rising branch of the Hadley circulation. *The Hadley Circulation: Present, Past and Future*, H. F. Diaz and R. S. Bradley, Eds., Advances in Global Change Research, Vol. 21, Springer, 121–152.
- , and S. G. H. Philander, 1994: A coupled ocean-atmosphere model of relevance to the ITCZ in the eastern Pacific. *Tellus*, **46A**, 340–350, <https://doi.org/10.3402/tellusa.v46i4.15484>.
- , and Y. Kosaka, 2017: What caused the global surface warming hiatus of 1998–2013? *Curr. Climate Change Rep.*, **3**, 128–140, <https://doi.org/10.1007/s40641-017-0063-0>.
- , H. Xu, N. H. Saji, Y. Wang, and W. T. Liu, 2006: Role of narrow mountains in large-scale organization of Asian monsoon convection. *J. Climate*, **19**, 3420–3429, <https://doi.org/10.1175/JCLI3777.1>.
- , and Coauthors, 2007: A regional ocean–atmosphere model for eastern Pacific climate: Toward reducing tropical biases. *J. Climate*, **20**, 1504–1522, <https://doi.org/10.1175/JCLI4080.1>.
- Xu, H., Y. Wang, and S.-P. Xie, 2004: Effects of the Andes on eastern Pacific climate: A regional atmospheric model study. *J. Climate*, **17**, 589–602, [https://doi.org/10.1175/1520-0442\(2004\)017<0589:EOTAOE>2.0.CO;2](https://doi.org/10.1175/1520-0442(2004)017<0589:EOTAOE>2.0.CO;2).
- , S.-P. Xie, Y. Wang, and R. J. Small, 2005: Effects of Central American Mountains on the eastern Pacific winter ITCZ and moisture transport. *J. Climate*, **18**, 3856–3873, <https://doi.org/10.1175/JCLI3497.1>.
- Xu, W., and J.-E. Lee, 2021: The Andes and the southeast Pacific cold tongue simulation. *J. Climate*, **34**, 415–425, <https://doi.org/10.1175/JCLI-D-19-0901.1>.
- , —, B. Fox-Kemper, Y. Planton, and M. J. McPhaden, 2022: The Andes affect ENSO statistics. *J. Climate*, **35**, 7077–7091, <https://doi.org/10.1175/JCLI-D-21-0866.1>.
- Yu, H., and M. Zhang, 2018: Explaining the year-to-year variability of the Eastern Pacific intertropical convergence zone in

- the boreal spring. *J. Geophys. Res. Atmos.*, **123**, 3847–3856, <https://doi.org/10.1002/2017JD028156>.
- Zhang, Q., B. Liu, S. Li, and T. Zhou, 2023: Understanding models' global sea surface temperature bias in mean state: From CMIP5 to CMIP6. *Geophys. Res. Lett.*, **50**, e2022GL100888, <https://doi.org/10.1029/2022GL100888>.
- Zhou, S., G. Huang, and P. Huang, 2020: Excessive ITCZ but negative SST biases in the tropical Pacific simulated by CMIP5/6 models: The role of the meridional pattern of SST bias. *J. Climate*, **33**, 5305–5316, <https://doi.org/10.1175/JCLI-D-19-0922.1>.
- Zhou, W., and S.-P. Xie, 2017: Intermodel spread of the double-ITCZ bias in coupled GCMs tied to land surface temperature in AMIP GCMs. *Geophys. Res. Lett.*, **44**, 7975–7984, <https://doi.org/10.1002/2017GL074377>.
- , L. R. Leung, and J. Lu, 2022: Linking large-scale double-ITCZ bias to local-scale drizzling bias in climate models. *J. Climate*, **35**, 7965–7979, <https://doi.org/10.1175/JCLI-D-22-0336.1>.